

Article

Chromite-Bearing Peridotite Identification, Based on Spectral Analysis and Machine Learning: A Case Study of the Luobusa Area, Tibet, China

Weiguang Yang ^{1,2,3}, Youye Zheng ^{2,4,*} , Shizhong Chen ^{1,3,5}, Xingxing Duan ^{1,3}, Yu Zhou ^{1,3} and Xiaokuan Xu ⁶

- ¹ Urumqi Comprehensive Survey Center on Natural Resources, China Geological Survey, Urumqi 830057, China; yangwg_cugb@126.com (W.Y.)
- ² School of Earth Sciences and Resources, China University of Geosciences, Beijing 100083, China
- ³ Innovation Base of Metallogenic Prediction and Prospecting in Central Asia Orogenic Belt, Chinese Geological Society, Urumqi 830057, China
- ⁴ Institute of Geological Survey, China University of Geosciences, Wuhan 430074, China
- ⁵ Nanjing Geological Survey Center, China Geological Survey, Nanjing 210016, China
- ⁶ Faculty of Science and Technology, University of Canberra, Canberra 2601, Australia
- * Correspondence: zhyouye@163.com

Abstract: Chromite is a strategic mineral resource for many countries, and chromite deposit occurrences are widespread in the ultramafic rocks of the Yarlung Zangbo ophiolite belt, particularly in the harzburgite unit of the mantle section. Conducting field surveys in complex and poorly accessible terrain is challenging, expensive, and time-consuming. Remote sensing is an advanced method of achieving modern geological work and is a powerful technical means of geological research and mineral exploration. In order to delineate outcrops of chromite-bearing mantle peridotite, the present research study integrates seven image-enhancement techniques, including optimal band combination, decorrelation stretching, band ratio, independent component analysis, principal component analysis, minimum noise fraction, and false color composite, for the interpretation of Landsat8 OLI and WorldView-2 satellite data. This integrated approach allows the effective discrimination of chromite-containing peridotite outcrops in the Luobusa area, Tibet. The interpretation results derived from these integrated image-processing techniques were systematically verified in the field and formed the basis of the feature selection process of different lithologies supported by the support vector machine algorithm. Furthermore, the distribution range of the ferric contamination anomaly is detected through the de-interference abnormal principal component thresholding technique, which shows a high spatial matching relationship with mantle peridotite. This is the first study to utilize Landsat8 OLI and WorldView-2 remote sensing satellite data to explore the largest chromite deposit in China, which enriches the research methods for the chromite deposits in the Luobusa area. Accordingly, the results of this investigation indicate that the integration of information extracted from image-processing algorithms using remote sensing data could be a broadly applicable tool for prospecting chromite ore deposits associated with ophiolitic complexes in mountainous and inaccessible regions such as Tibet's ophiolitic zones.

Keywords: remote sensing; spectral enhancement techniques; support vector machine; mantle peridotite; chromite deposit



Citation: Yang, W.; Zheng, Y.; Chen, S.; Duan, X.; Zhou, Y.; Xu, X. Chromite-Bearing Peridotite Identification, Based on Spectral Analysis and Machine Learning: A Case Study of the Luobusa Area, Tibet, China. *Appl. Sci.* **2023**, *13*, 9325. <https://doi.org/10.3390/app13169325>

Academic Editor: Andrea L. Rizzo

Received: 12 May 2023

Revised: 28 July 2023

Accepted: 10 August 2023

Published: 17 August 2023



Copyright: © 2023 by the authors. Licensee MDPI, Basel, Switzerland. This article is an open access article distributed under the terms and conditions of the Creative Commons Attribution (CC BY) license (<https://creativecommons.org/licenses/by/4.0/>).

1. Introduction

Ophiolite hosts economic minerals such as chromium, which explains why chromite deposit exploration attempts for ore resources have resulted in much research interest by scientists and exploration geologists across the world. Ophiolitic ultramafic rocks are the hosts of podiform chromite deposits. Chromitite is closely associated with mantle peridotite in ophiolitic complexes [1]. Ophiolite zones in Tibet are widespread and are often found in

different locations with varying geologic and tectonic settings. The Luobusa ophiolite is one of the most promising areas for prospecting chromite deposits because of the extensive outcrops of mantle peridotites [2]. Dozens of chromite deposits have been identified in mantle peridotite. These chromite occurrences have lenticular, tubular, and vein-like shapes, a few meters or tens of meters in length, which are hosted in peridotites. These bodies are individually small, but, where abundant, they form large-scale chromite deposits [3]. Accordingly, the discrimination and mapping of mantle peridotites in ophiolitic complexes are quite interesting for chromite exploration plans.

The Luobusa chromite deposit is a typical ophiolite-type or alpine-type chromite deposit, also known as a podiform chromite deposit due to its production characteristics. It is the largest and highest-quality chromite deposit in China [4,5]. Although its cumulative reserves of more than 500×10^4 t still cannot compare with the known super-large chromite deposits in the world (100 Mt), such as Bushveld in South Africa and Kempirsai in the Southern Urals, its prospects should not be underestimated [2,6]. Moreover, the ore quality (grade) of the Luobusa chromite deposit is excellent, with the content of Cr_2O_3 in the ore generally as high as 50%, and $\text{Cr}_2\text{O}_3/\text{FeO} > 4$ [7–9]. Therefore, due to the great extent of ultramafic rocks, which are the host of chromite deposits in the Luobusa ophiolite, the possibility of discovering new chromite deposits is high, and more exploration and investigation is needed. There is reason to believe that its reserves can be increased through continued exploration [2,9,10].

However, most Tibet ophiolitic zones are located in mountainous and inaccessible regions. Thus, given that the outcrop scale of ophiolite is often large, and traditional geological surveys are more expensive, time-consuming, and inefficient, especially for geological environments with high altitudes and harsh conditions that make it difficult to form a comprehensive understanding, new exploration methods such as the remote sensing method can be useful for this purpose [11–13]. Remotely sensed data have been extensively used for the delineation of lithological units and geological mapping. In contrast to conventional field surveying, remote sensing, with its macro, comprehensive, multi-scale, and multi-level characteristics, has become an effective tool for lithology mapping and has been widely used in geological work at different spatial scales [14–19]. Each multispectral band records unique energy interactions with a surface, and geological features are enhanced spectrally (such as band ratio (BR), principal component analysis (PCA), independent component analysis (ICA), minimum noise fraction (MNF), and RGB color combinations) and spatially (such as image fusion and filtering), thereby improving their tones, hues, image texture, fracture patterns, lineaments, and trends to distinguish the different lithologic units. Image-enhancement methods produce new images with detailed information from the highly correlated bands. In different countries and regions, previous studies have performed a lot of work using remote-sensing technology for ophiolite delineation [15,20–25]. Currently, geological mapping techniques have combined with machine learning, such as a support vector machine (SVM). Several geologists have made remote sensing data more effective in lithological and mineral mapping by employing advanced machine-learning algorithm techniques [26–28]. The spectral bands of the multispectral sensor are characteristic for absorptions of such minerals, and thus the bands of the sensor can be used to discriminate the ferric iron-rich weathered surfaces of harzburgites [29].

In the field of remote-sensing technology used to delineate ophiolite, previous research mostly focused on two or three spectral enhancement approaches or a single data source. Consequently, the current study combined remote-sensing data (Landsat8 and WorldView-2) of different resolutions, processed the integration of seven image enhancement techniques, and analyzed the utilization of the support vector machine algorithm (SVM) and anomaly extraction technique for mantle peridotites, delineating and extracting alterations in the Luobusa area for the first time.

2. Geological Setting

The chromite-bearing ophiolite belt in Tibet is mainly located in the Yarlung Zangbo deep fault [8,30,31]. The Lhasa block is located in Yarlung Zangbo ophiolite belt in the eastern part of the Tethys-Himalayan tectonic belt and is regionally controlled by the Indus-Yarlung Zangbo suture zone, bordered by the Gangdese-Nyainqentanglha tectonic belt to the north and the Himalayan tectonic belt to the south [32,33] (Figure 1a,b). Due to the superimposition of the Himalayan orogeny and a series of fault structures, the ophiolites have been modified by late tectonic activity, and the massifs on both sides of the north–south axis are limited by faults [30,34]. The massifs form a south-dipping wall-shaped complex, with the northern part composed of Paleogene–Neogene conglomerate and the new Cenozoic Gangdese granite, and the southern part composed of late Triassic metamorphic slate, sandstone, and phyllite (Figure 1c) [34,35].

The Lhasa massifs extend nearly east–west and have a planar shape that is an inverted “S” shape [36,37]. The chromitite orebodies are grouped into three clusters, designated from west to east, the Luobusa, Xiangkashan, and Kangjinla districts [1,6,38]. The ophiolitic section forms a tectonic slab, made up primarily of mantle peridotites with minor crustal cumulates and mafic dikes. The mantle rocks constitute ~93% of the exposure section and include harzburgite and less dunite. Both the drill core and surface samples indicate that the peridotites consist chiefly of harzburgite. Most of the harzburgites, both in the outcrop and drill core, are fresh, dark green, and massive. The rocks mostly have coarse-grained, granular textures and consist chiefly of olivine (68~85 modal%) and orthopyroxene (14~30%) with minor clinopyroxene, magnesiochromite, and magnetite [1]. The cumulate rocks consist of wehrlite, lherzolite, pyroxenite, and gabbro [1,34,35,39].

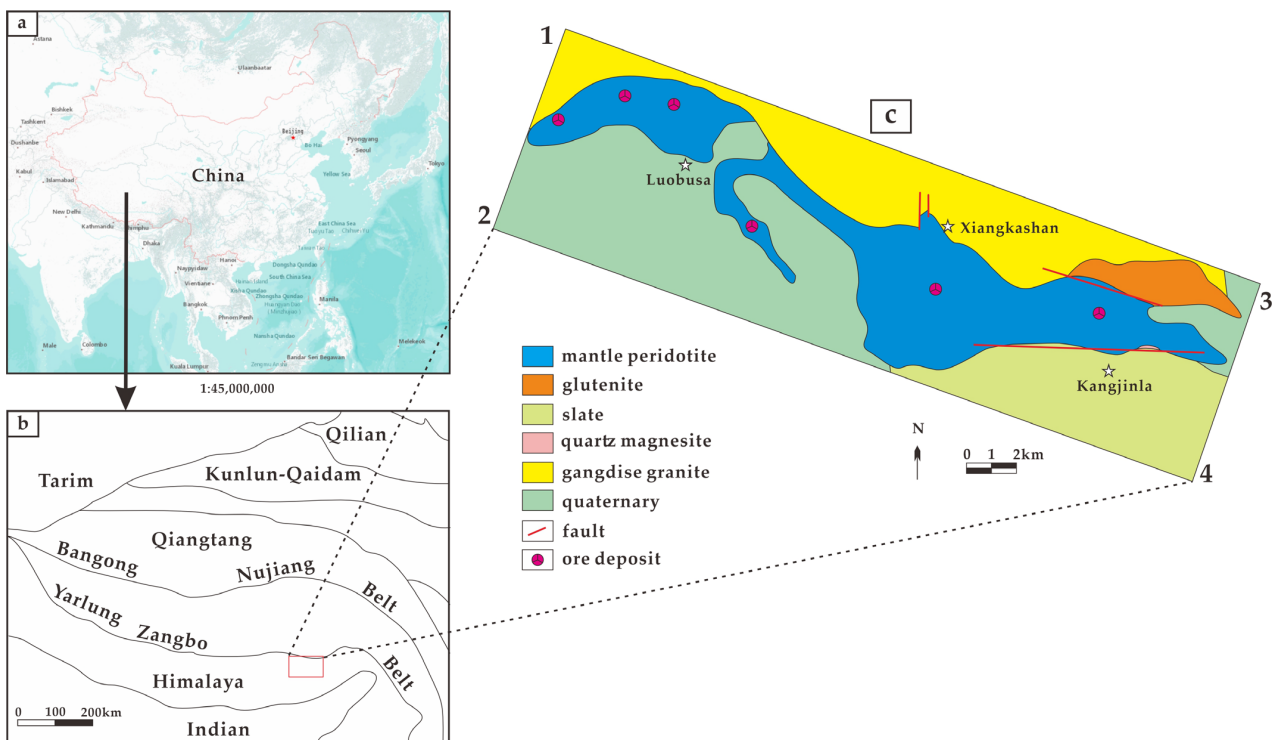


Figure 1. (a) The study area is located in China’s geographical location; (b) tectonics in the study area, adapted from Ref. [40]; (c) a geological map of the study area is shown on the right, which was derived from an initial geological map at 1:50,000. The geological map is not shown strictly in accordance with the criteria, but in other bright and easily distinguishable colors to more clearly show the spatial distribution and boundaries of litho-units. The extent defined by corner points (1) 29°14′40″ N, 92°10′35″ E; (2) 29°12′24″ N, 92°9′31″ E; (3) 29°11′47″ N, 92°19′41″ E; (4) 29°9′29″ N, 92°18′47″ E.

Chromite deposits are mainly hosted in mantle peridotite and appear in groups and belts, which is typical of alpine-type chromitite deposits [6]. Most of the orebodies lie near the top of the mantle section [41]. The structure of chromite ore includes blocky, beany, banded, and impregnated shapes (Figure 2). The main characteristic of the ore is that it is rich in Cr_2O_3 and associated with platinum group elements, mainly osmium and ruthenium, which can be comprehensively utilized [2]. Mantle peridotite is an exclusive rock for podiform chromite deposits, and chromite is closely associated with the mantle peridotite belt, so the chromium needed for chromite may mainly come from mantle peridotite itself [4,38,42]. Furthermore, previous studies have shown that the chromium content in the mantle and in chondrite meteorites is much higher than that in the crust, and ultra-high-pressure minerals from the deep mantle, such as diamonds, have been found in the Luobusa chromite deposits, providing important information on the deep-seated genesis of chromite [1,5,6,35,43–45].

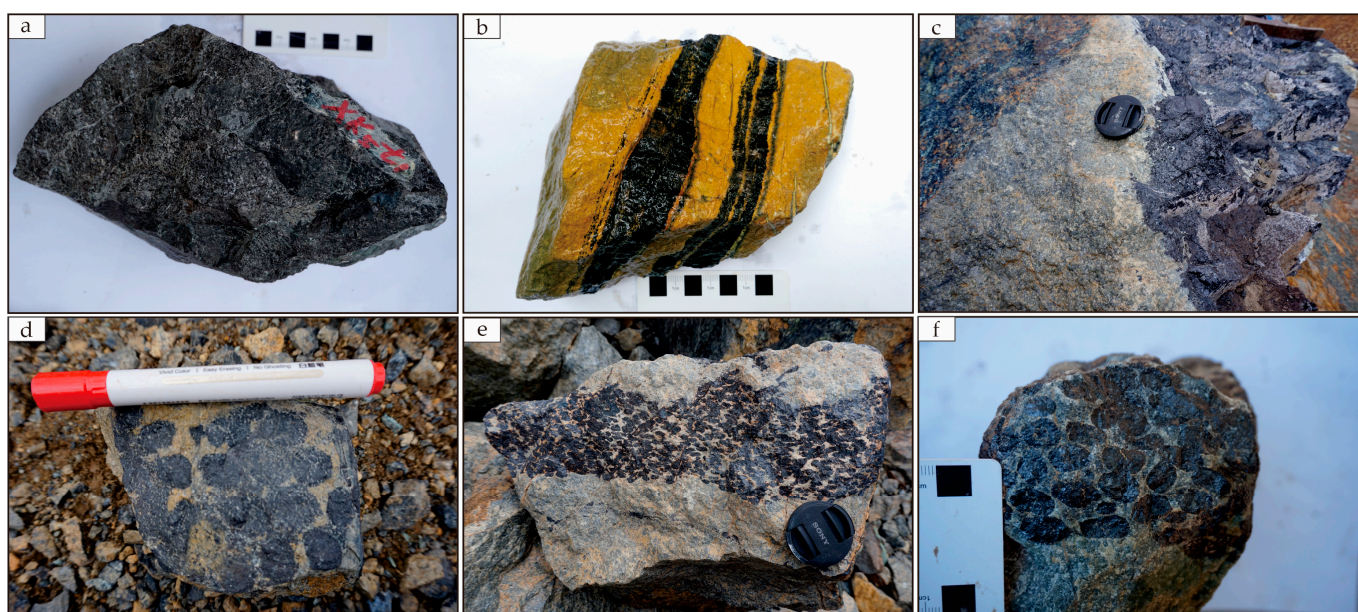


Figure 2. Field photographs of typical ore structures of (a) chromitite with massive ore; (b) banded chromite; (c) densely disseminated chromitite; (d–f) well-developed nodular chromitite.

3. Data Sources

This article uses Landsat8 OLI and WorldView-2 remote-sensing data, and its basic parameters are shown in Table 1. Landsat8 carries two sensors: OLI and TIRS. The OLI sensor includes nine bands of a spatial resolution of 30 m, including a panchromatic band of a spatial resolution of 15 m [46]. OLI includes all the bands of Landsat7 ETM+ and has a narrower spectral width, which improves the recognition quality of clay minerals and iron oxides and can better distinguish vegetation and non-vegetation features in the panchromatic image. In order to avoid atmospheric absorption features, OLI Band 5 excludes the water vapor absorption feature of $0.825\ \mu\text{m}$. In addition, a blue band (band 1: $0.433\text{--}0.453\ \mu\text{m}$) and a cirrus band (band 9: $1.360\text{--}1.390\ \mu\text{m}$) are added, which can be applied to coastal observation and cloud detection, respectively. Furthermore, all the OLI and TIRS spectral bands are stored as geolocated 16-bit digital numbers in the same Level 1 terrain corrected (L1T) file, which facilitates the differentiating of materials more efficiently than ETM+ imagery stored as 8-bit numbers [47,48]. Although multispectral sensors such as TM, ETM+, and OLI render insufficient spectral resolution for discriminating specific minerals, achieving effective processing, or running data analysis, they yield useful image products for regional exploration and discovery when they are combined with a good understanding of the associated landforms [46]. In this study, a cloud-free L1T Landsat-8

image of the study area (path/row 137/40) was downloaded from the US Geological Survey (USGS) Earth Resources Observation and Science Center (<http://earthexplorer.usgs.gov>).

Table 1. Characteristics of Landsat8 and WorldView-2 data.

Satellite	Band	Range/ μm	Resolution/m	Swath Width/km	Altitude/km	Launch Date
Landsat8	B1 Coastal	0.43–0.45				
	B2 Blue	0.45–0.51				
	B3 Green	0.53–0.59				
	B4 Red	0.64–0.67	30			
	B5 NIR	0.85–0.88				
	B6 SWIR 1	1.57–1.65		185	705	February 2013
	B7 SWIR 2	2.11–2.29				
	B8 Pan	0.50–0.68	15			
	B9 Cirrus	1.36–1.38	30			
	B10 TIR 1	10.6–11.19				
	B11 TIR 2	11.5–12.51	100			
WorldView-2	B1 Coastal	400–450				
	B2 Blue	450–510				
	B3 Green	510–580				
	B4 Yellow	585–625				
	B5 Red	630–690	1.84	16.4	770	October 2009
	B6 Red edge	705–745				
	B7 NIR 1	770–895				
	B8 NIR 2	860–1040				
Pan	450–1040	0.46				

NIR = visible near infrared, SWIR = short-wave infrared, and TIR = thermal infrared.

The WV-2 satellite was launched on 6 October 2009 and operates on a sun-synchronous orbit at a height of 770 km [49]. It can provide panchromatic imagery with a spatial resolution of 0.5 m and multi-spectral high-resolution satellite imagery with a spatial resolution of 1.8 m [50,51]. The satellite-borne multispectral sensor not only has four standard spectral bands of the industry (red, green, blue, and near-infrared 1), but also includes four additional bands (coastal, yellow, red edge, and near-infrared 2) [52–54]. The data used in this article were imaged on 8 February 2015.

The remote sensing images are clear, with a strong sense of hierarchy for different land cover types, clear textures, and good tone contrast. The projection coordinate system is the UTM Mercator projection, and the ellipsoid is WGS-84.

4. Methodology

In this article, two types of data were preprocessed, including orthorectification, radiometric calibration, atmospheric correction, cropping, and image fusion. Then, seven spectral processing methods were comprehensively applied to OLI and WV-2 images to enhance the color differences between various lithologies. The advantage of high spatial resolution was fully utilized to establish the main lithological interpretation signs. By establishing training samples, effective supervised classification of OLI images was performed using the support vector machine algorithm, and the “de-interference anomaly principal component thresholding technology” was used to extract abnormal information. Finally, remote-sensing images were comprehensively evaluated and verified in the field. The image-processing operations were completed using ENVI 5.6 and ArcGIS pro3.0 software, as shown in the technical flowchart in Figure 3.

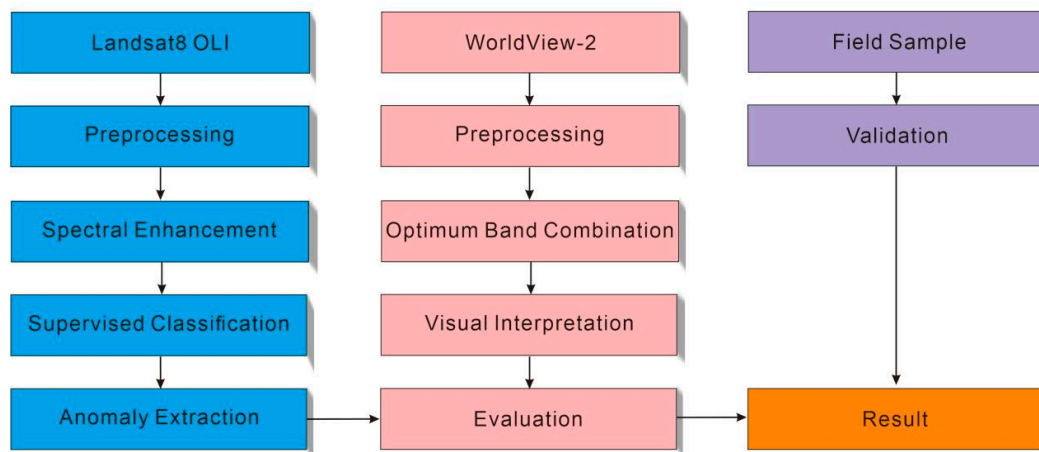


Figure 3. Flowchart showing the data used and methodology followed in the current study.

4.1. Image Preprocessing

Orthorectification was applied to the WorldView-2 data, using a small number of ground control points combined with the satellite model to correct spatial and geometric distortions in the image. Remote sensing images generally record information in digital quantization values (DN) without quantization scales, and we need to use radiometric calibration to convert DN values into specific physical quantities (radiance, reflectance). Radiometric calibration establishes a quantitative relationship through the linear equation $L_{\lambda} = \text{Gain} \times \text{DN} + \text{Offset}$ (where Gain is the sensor gain value, and Offset is the offset value) [55]. Then, the Fast Line-of-sight Atmospheric Analysis of Spectral Hypercubes (FLAASH) atmospheric correction algorithm was used to eliminate or reduce the influence of atmospheric scattering on the reflectance of the land surface, to obtain the true reflectance of the land cover. It is based on the MODTRAN5 radiation transfer model and is currently the most accurate atmospheric correction method under ENVI software. In many studies, it has been proven to be significantly effective in removing atmospheric effects [56–61]. The fusion method used the super-resolution Bayesian fusion algorithm, namely, Gram–Schmidt Pan Sharpening, which is currently one of the best remote-sensing fusion algorithms in terms of fusion effect and color fidelity. Its advantages lie in automatic alignment, retaining spectral information, and increasing spatial resolution to enrich land cover information [62–64].

4.2. Digital Image Processing

For remote-sensing images, using multiple spectral enhancement techniques helps to contrast the range of lithology or highlight the boundaries of lithological units. In this paper, we combined seven spectral enhancement techniques, including optimal index analysis, decorrelation stretch, band ratio, independent component analysis, principal component analysis, minimum noise fraction, and false color composite.

4.2.1. Optimal Index Analysis

The optimal index method analyzes all RGB color combinations based on the total variance and correlation coefficients of multispectral remote-sensing data. Currently, the most widely used method for selecting the best bands is the optimal index factor (OIF) method, which comprehensively considers the information content of single-band images and the correlation between different bands [65,66]. It is closer to the basic principle of band selection, and the calculation is simple and easy to implement [62,67]. The formula for calculating OIF is $\text{OIF} = \sum_{i=1}^3 S_i / \sum_{j=1}^3 |R_{ij}|$, where S_i is the standard deviation of the i -th band, and R_{ij} is the correlation coefficient between the i -th and j -th bands [68,69]. OIF sorts all possible RGB band combinations generated from remote-sensing images, and the band with the highest OIF value usually has the most information.

4.2.2. Decorrelation Stretch (DS)

Decorrelation stretch (DS) is a type of color stretch used to solve the problem of overly concentrated image tone changes or decreased image saturation. It reduces the correlation between spectra and is widely used as a means of spectral enhancement [23,70,71]. For example, Abram used the 7-5-4 band decorrelation stretch with TM data to identify ultrabasic rocks when mapping the Oman ophiolite [22].

4.2.3. Band Ratio (BR)

Band ratio (BR) is one of the commonly used image-enhancement techniques [72,73]. It is a simple and helpful technique for reducing the effect of topography and enhancing the subtle differences in the spectral reflectance characteristics of rocks and soils [20,74]. Several band ratios and false color composites of ETM+ in RGB have been suggested for enhancing lithology and alteration zones, for example, 5/7 for hydroxyl-bearing minerals and 3/1 for iron oxide [57,61,71,75–79]. Many previous studies have used band ratios to identify mantle peridotites. For example, Sultan used an ETM (5/7, 5/1, 5/4 × 3/4) false-color image to delineate ultrabasic and basic rocks from silica-rich granitic rocks [24].

4.2.4. Principal Component Analysis (PCA)

Principal component transformation is a statistical technique that selects uncorrelated linear variables called principal components (PC) using orthogonal transformation of a set of possibly correlated variables [12,48,61,69,80–82]. It is one of the most effective and commonly used image information extraction methods in remote-sensing geology [12,48,61,69,80–82]. It generates very small and easily interpretable independent components through linear transformation and preserves the main information [12,48,61,69,80–82]. The first principal component includes most of the information of the original multispectral image, and selecting three transformed principal components for the false color composite can achieve the purposes of data compression and highlighting of target information.

4.2.5. Independent Component Analysis (ICA)

Independent component analysis transforms a set of mixed signals into independent components and statistically estimates the maximum correlation direction, which can reduce losses in the data decomposition process [69,83–87]. It can be considered a special case of principal component analysis (PCA).

4.2.6. Minimum Noise Fraction (MNF)

Minimum noise fraction (MNF) is an orthogonal transformation that is a very useful algorithm for reducing the inherent dimensionality of multispectral data and reducing noise in images [23]. MNF is essentially two cascaded principal component transformations, where the first transformation is used to separate and rescale the noise in the data, and the second transformation is the standard principal component transformation of the noise-whitened data [56]. MNF transformation is also commonly applied directly to vegetation or lithological mapping [46,69,71,79,88].

4.2.7. False Color Composite (FCC)

False color images can greatly facilitate image visualization for better interpretation. In this study, the selection of the RGB combination method was mainly based on the rock types and their spectral characteristics, the geological information carried by each spectral transformation component, and previous research experience. RGB false color synthesis was used to highlight the differences in tone of various lithological units.

4.3. Machine Learning Classification

Recently, using machine learning methods in geoscience studies has been increasing in various applications, including mapping land-cover types and monitoring land usage.

Some work has been carried out in the field of identifying and classifying lithologies of valuable minerals [56].

Digital image classification by computers can greatly improve the objectivity of the image classification process. The the support vector machine algorithm (SVM) method is widely used in machine learning methods for geological applications, and it has proven to be robust and effective, especially in helping in the identification of rock units over the years [26–28,77,89].

Supervised classification is a machine learning method based on statistical learning theory (SLT), which is based on the theory of statistical learning and the principle of structural risk minimization [90,91]. The basic strategy is to find an optimal hyperplane that can separate the two classes of data and use confirmed sample units to identify unknown class pixels [18,92]. It automatically seeks support vectors that have greater discriminative power for classification based on limited sample information and maximizes the gap between classes [27,28]. Compared to other traditional supervised classification methods in geological surveys, it has been confirmed to deliver higher classification accuracy than other traditional supervised classification schemes [93–95].

4.4. De-Interfered Anomaly Principal Component Thresholding Technology

Principal component analysis (PCA) is a widely used and mature technique for extracting anomalous information. This paper uses the “De-interfered Anomaly Principal Component Thresholding Technology”, which has been determined by the China Geological Survey as a remote-sensing technology method that must be used in mineral survey work [96,97]. In a pixel, as long as the vegetation does not exceed 50%, anomalous information can be extracted. After performing principal component transformation on the selected bands, the threshold of 2, 3, and 4 is set based on the variance σ of the anomaly intensity as the scale to achieve density segmentation of the anomaly principal components. To present the anomaly image more intuitively, the density segmentation result also needs to be processed with a 5×5 Gaussian low-pass filter.

5. Results and Discussion

5.1. Image Enhancement Results

5.1.1. OIF

Due to the spectral mixing effect and fuzziness of spectral features in low spatial resolution of satellite images, for the lithological interpretation of WV-2 data, we assigned more weight to visual inspection and interpretation to establish interpretation signs. We took full advantage of its spatial resolution and avoided the disadvantage of its narrow spectral range. For visual interpretation, the difference between hues is the most significant and intuitive. Based on the data correlation analysis of WV-2, it can be known that the optimal index value for the combination of b8, b6, and b4 is the largest (Table 2), and selecting these three bands is more conducive to the interpretation of lithology and structure. However, in actual remote-sensing interpretation, other combination schemes can also be used, such as selecting b5-b3-b2 for true color synthesis to make the image closer to natural colors, or selecting b7-b5-b3 for standard false color to show vegetation in characteristic red.

Sedimentary rocks in the area are mainly composed of compound conglomerate, sandstone, siltstone, and significant banded texture structure is a typical remote-sensing interpretation sign [62]. Combined with the comprehensive characterization of rock texture and hue, the identification and delineation of sedimentary rocks in the study area can be achieved. At the macroscopic scale, conglomerate is characterized by multiple steep slopes, with large terrain undulations, underdeveloped water systems and vegetation, and rough texture (Figure 4a). Sandstone generally exhibits a more typical parallel banded texture on high spatial resolution images, with relatively delicate image features distinguishing it from conglomerate (Figure 4b). As a microclastic rock, siltstone appears delicate and soft in the WV-2 image. The WV-2 of b5-b3-b2 in RGB separated siltstone into brown-yellow, black-gray, and gray-brown (Figure 4c). Because this type of rock has poor water permeability,

typical branched water system textures can be seen in the WV-2 image, and the vegetation is relatively developed.

Table 2. Optimal index factor and index highest rankings of WV-2 bands.

	R	G	B	OIF
	8	6	4	255.29
	8	6	3	250.57
	8	6	1	229.29
	8	4	1	221.34
	7	6	1	218.71
	8	3	1	213.14
	7	4	1	209.53
	7	5	3	203.96
	8	5	1	198.60
	7	5	1	184.75

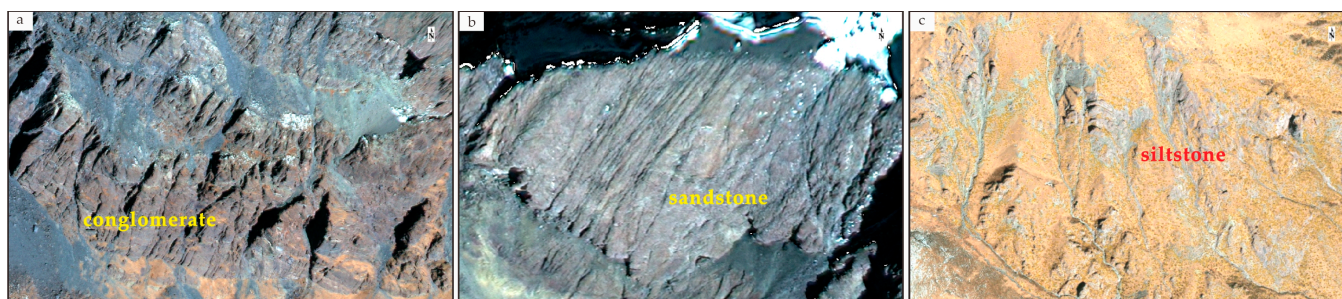


Figure 4. WV-2 images of sedimentary rocks: (a) conglomerate, RGB: 864; (b) sandstone, RGB: 864; (c) siltstone, RGB: 532.

Most metamorphic rocks are characterized by relatively uniform hue and monotonous and directionally arranged discontinuous textures [62]. Common metamorphic rocks in the area include slate, quartz-magnesite rocks, and marble. The Upper Triassic slate is the most common metamorphic rock in the study area and has obvious interpretation signs. Due to the low degree of metamorphism in slate, it retains many features of microclastic rock, with finer residual slope sediments and low gentle hills or hill-like terrain (Figure 5b). The hue is mainly gray or black, and the distribution is mainly in the northeast part of the study area (Figure 5a). The boundary between the quartz-magnesite rock and the slate is neat, intermittently exposed along the southern boundary of the ophiolite body, and the north part of it is strongly developed with serpentinization (Figure 5c). The interpretation sign of marble is similar to carbonate rocks. In this article, the WV-2 true color synthesis of b5-b3-b2 in RGB with grayish and light colors as the main hue, with many speckled texture features, steep terrain, and retaining the basic characteristics of limestone (Figure 5d).

The mantle peridotites crop out in a broad band along part of the ophiolite and make up the bulk of the ophiolite; harzburgite accounts for 70% of the Luobusa mantle peridotite [1]. The interpretation and delineation of ultramafic rocks using high-resolution remote-sensing images are more based on comprehensive analysis and judgment. Most of the chromitite bodies in Luobusa are located in the harzburgite; we focus on mantle peridotites closely related to chromite deposits. The harzburgites are locally deformed and serpentinized, particularly those in the eastern part of the ophiolite. Alteration increases slightly near the chromitite orebodies, and both serpentinite and tectonic breccias are locally present [1]. The dark minerals of mafic and ultramafic were easily faded by weathering, and the surface developed serpentinization. They often appeared in negative terrain, and the residual slope developed. In order to intuitively identify the target objects in WV-2 images according to the tones and texture characteristics of peridotite in the study area, B5, B3, and B2 were selected and placed in channel R, G, and B, respectively, to reflect

the actual color characteristics, so as to better identify light green weathered peridotite (Figure 6a) and serpentinized peridotite with a light green tone (Figure 6b).

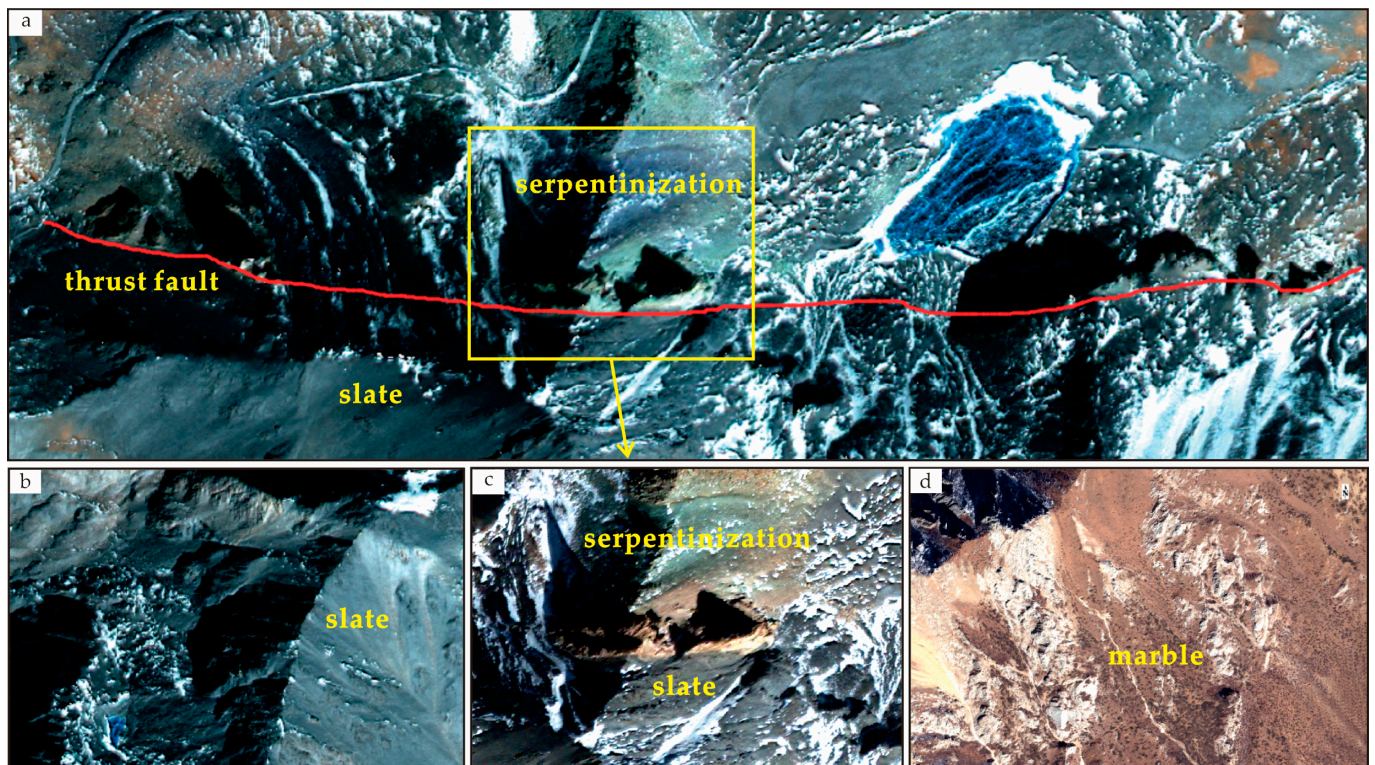


Figure 5. WV-2 images of metamorphic rocks: (a) regional image, RGB: 864; (b) slate, RGB: 864; (c) serpentinization, RGB: 532; (d) marble, RGB: 532.

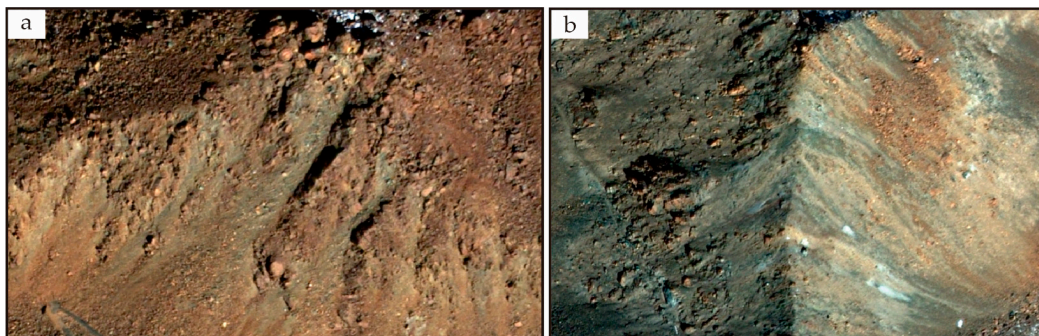


Figure 6. WV-2 images of peridotite: (a) peridotite; (b) serpentinized peridotite.

5.1.2. Band Ratio (BR)

The reflectance spectrum of a rock depends on the mineralogical composition of its surface, which is usually a mixture of the whole rock mineralogy and weathering minerals. Accordingly, the selected bands in this technique depend on their spectral reflectance and the positions of the absorption bands of the mineral being detected. Therefore, the presence of ferrous iron (Fe^{2+}) on weathered surfaces produces absorptions centered at about 0.45 μm , 1.0–1.1 μm , 1.8–1.9 μm , and 2.2–2.3 μm , depending on its lattice environment. The ferric iron (Fe^{3+}) produces absorptions at about 0.65 μm and 0.87 μm [61]. Based on the spectral absorption and reflection characteristics of harzburgite, this study selected the b5/b4 and b4/b7 band ratios. The operation process is to divide the grayscale values of corresponding pixels into two different band images, which can effectively suppress the topographic changes in the Tibetan mountain area and highlight the information of exposed rocks. The

differences between objects with significantly different spectral characteristics are easily recognizable in false color composite images [29,60,98–101]. The final results of the b5/b4, PC4, and b4/b7 RGB images showed exquisite contrasts between different rock units in the study area (Figure 7). This contrast enabled better detection of the mantle peridotite as a dark blue color, sandstone presented as green, and slate presented as light blue. We believe that band-ratio combinations proved their effectiveness in lithological mapping due to their shown ability to highlight spectral properties of specific rocks and minerals, while eliminating or reducing other types of information.

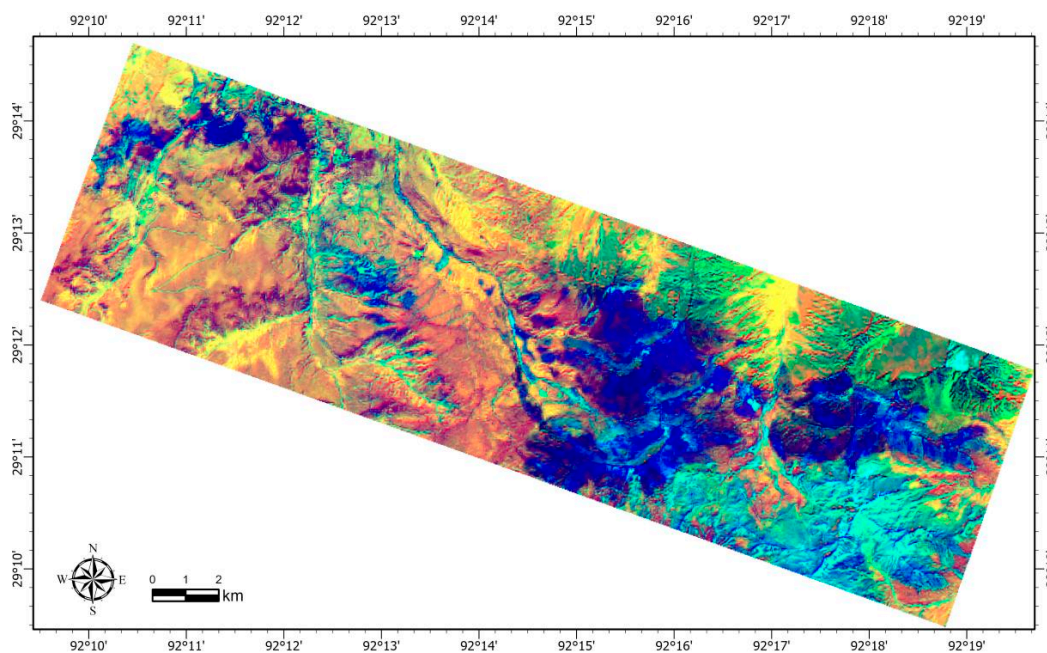


Figure 7. Lithological discrimination using OLI band-ratio color composites of b5/b4-PCA4-b4/b7 in RGB.

5.1.3. Principal Component Analysis (PCA) and Independent Component Analysis (ICA)

PCs contain spectral information relative to minerals and whether the digital numbers (DNs) of pixels containing the target minerals had high (bright) or low (dark) values [61]. In this article, PC1 tends to represent topographic and brightness information, while PC4 may represent the characteristic information of a lithology with low DN. Although lower-order principal components only contain a small amount of spectral information, they have a lower signal-to-noise ratio. Therefore, selecting lower-order and higher-order principal components for combination is very meaningful for emphasizing some target spectral features [72,87,98,102–104]. We selected PC6, PCA5, PCA4, and PCA2 components for RGB false color composites, which can better distinguish mantle peridotite rocks from other lithological units. The RGB combinations of PCA5-PCA4-PCA2, PCA2-PCA4-PCA5, and PCA6-PCA4-PCA2 demonstrated the distribution of mantle peridotite in blue or purple where it was prominently emphasized (Figure 8a–c). Meanwhile, the main IC component obtained by independent component transformation and the main PC component band combination were used to maximize the expression of component information. Results revealed that combining ICA1-ICA7-ICA6 in the RGB channels enhanced not only the differentiation of mantle peridotite in a red color but also the identification of southeast slate in a viridis color (Figure 8d).

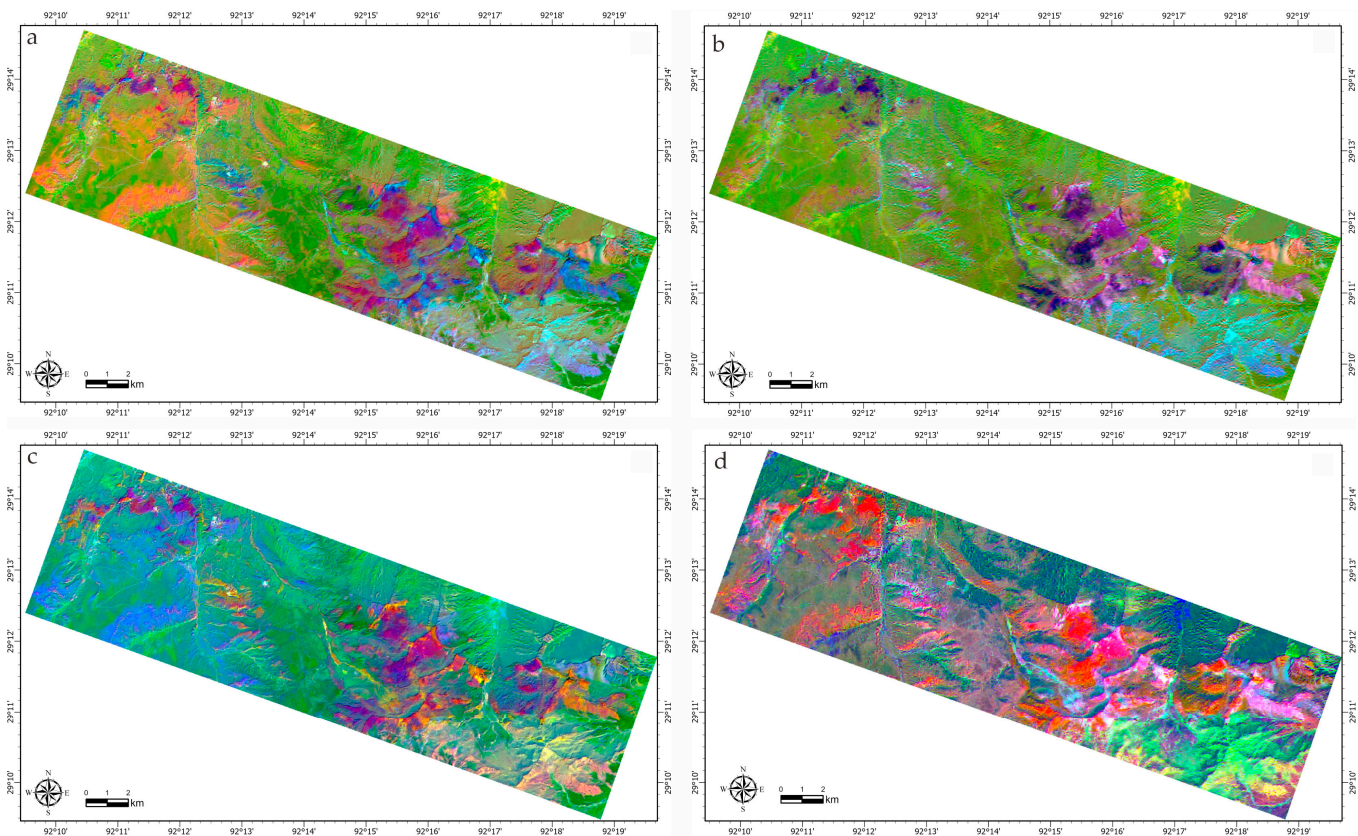


Figure 8. Lithological discrimination using OLI principal component analysis of (a) PCA5-PCA4-PCA2; (b) PCA6-PCA4-PCA2; (c) PCA2-PCA4-PCA5; and (d) ICA1-ICA7-ICA6 in RGB.

5.1.4. Minimum Noise Fraction (MNF) and Decorrelation Stretch (DS)

In this study, our results revealed that the MNF5 represents mantle peridotite information and MNF3 represents topographic information. Therefore, we selected MNF3-MNF5-MNF2 and placed them in the RGB channel, respectively; the RGB image showed an exquisite contrast between different rock units in the study area. This contrast enabled better detection of the range of ophiolitic mantle peridotite as fluorescent green in color (Figure 9a). Other geological units, such as conglomerate, were purple in color, mainly distributed in the northeast corner of the study area and distinguished from the Gangdese granite based on texture features, and metamorphic slate in brown in the southeast corner of the image. Moreover, using the MNF bands as inputs for the decorrelation stretch technique results in convenient discrimination for all the exposed rock units through DS of b7-MNF5-MNF3 FCC in RGB (Figure 9b). Their combined composite delivered images with better saturation and color contrast.

5.1.5. False Color Composite (FCC)

As dimensionality reduction and image-enhancement techniques, PCA and ICA transformations generate information-dense bands ideal for identifying the spectral features of minerals or rock units within the study area. Although principal component analysis (PCA) or minimum noise fraction (MNF) can compress and separate overlapping information, the lithological information we focus on often concentrates on the later components after performing PCA or MNF transformation. Therefore, practical applications, by means of combining different components obtained by diverse methods, can yield better results than using a single transformation method. The combined ICA-PCA technique demonstrates higher noise suppression capabilities compared to using ICA or PCA separately. Using PCA4 and ICA2 in FCC PCA4-PCA4-ICA2 in RGB (Figure 10a) provides excellent identification of the mantle peridotite, where it separates the boundaries of mineralized

lithological units in blue. Additionally, the OLI RGB combination of ICA2-MNF5-PCA4 demonstrated mantle peridotite in purple-red in color (Figure 10b).

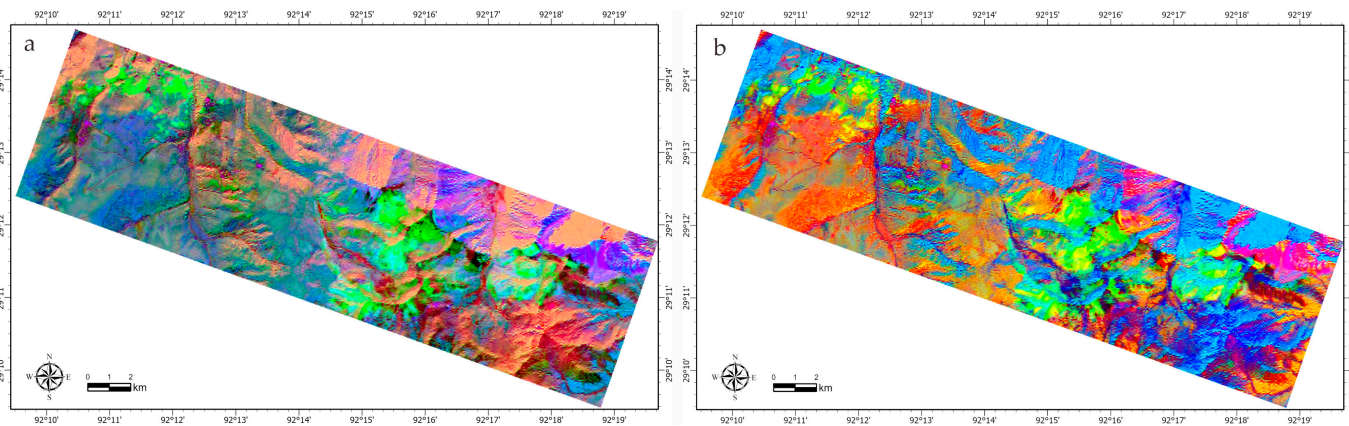


Figure 9. Lithological discrimination using OLI minimum noise fraction of (a) MNF3-MNF5-MNF2; (b) B7-MNF5-MNF3 in RGB.

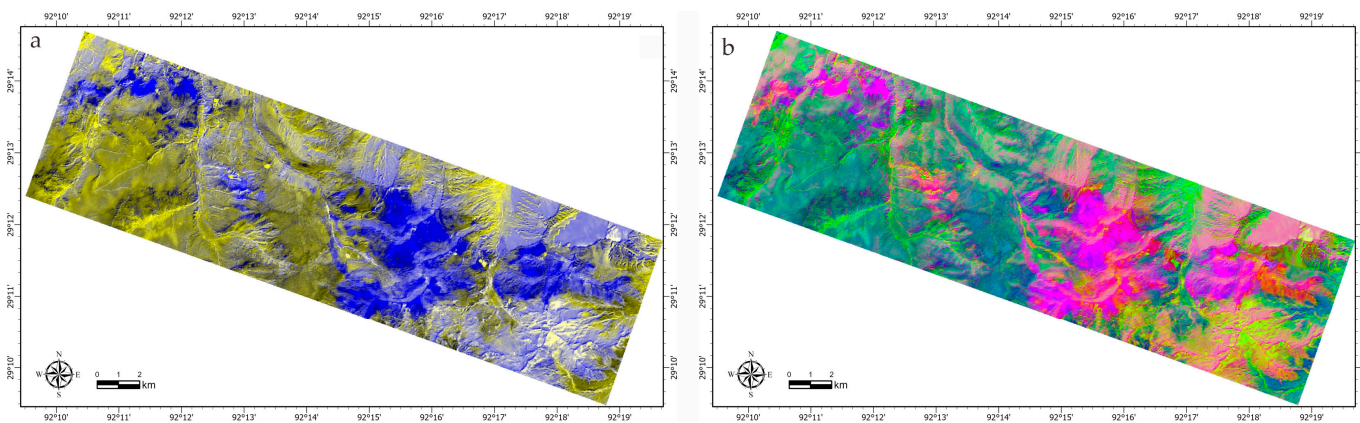


Figure 10. Mantle peridotite discrimination using OLI false color composites of (a) PC4-PC4-IC2; (b) ICA2-MNF5-PCA4 in RGB.

5.2. Machine Learning Results

Interference factors during image formation often make it difficult to achieve accurate classification of targets. Ensuring adequate training and testing data, besides selecting a suitable classifier, are the main pillars for delivering veracious classification. Toward that aim, the outputs of all the previously mentioned image-processing techniques, the spectral signatures of the different rock units, previous mapping, and field observations have been used as inputs for lithological classification utilizing the support vector machine algorithm. Consequently, for a more accurate selection of training sites in this study, three files were used: (1) all lithological data from compiled previous geological maps; (2) several effective RGB color composites resulting from various image-processing techniques, such as OIF, BR, PCA, and MNF; (3) the locations of rock samples.

The sample types in the study area are divided into seven categories: mantle peridotite, glutenite, slate, Gondwana granite, quaternary, water body, and hillshade. Accordingly, training areas for seven classes were determined and fed into the SVM algorithm. A total of 11,423 pixels representing seven targets were selected. The separability of each category exceeds 1.9. Secondly, by creating training samples from the region of interest (ROI) and using the support vector machine classification (SVM) method (algorithm) to classify the entire image, each pixel is merged into the known sample category created in advance. After classification, the Majority tool is used to remove small patches in the classified image

(Figure 11). Finally, these results are evaluated and compared using the overall accuracy and Kappa coefficient. The Kappa coefficient is distinct from the overall accuracy since it considers the complete contingency matrix and is intended to evaluate the consistency of the results [69,86]. The classification accuracy is evaluated using a confusion matrix, and the results shows overall classification accuracy of 94.98% and a Kappa coefficient of 0.93. However, misclassification still occurs in some areas, which is due to the mixed pixels caused by spectral resolution. Hence, field verification is required.

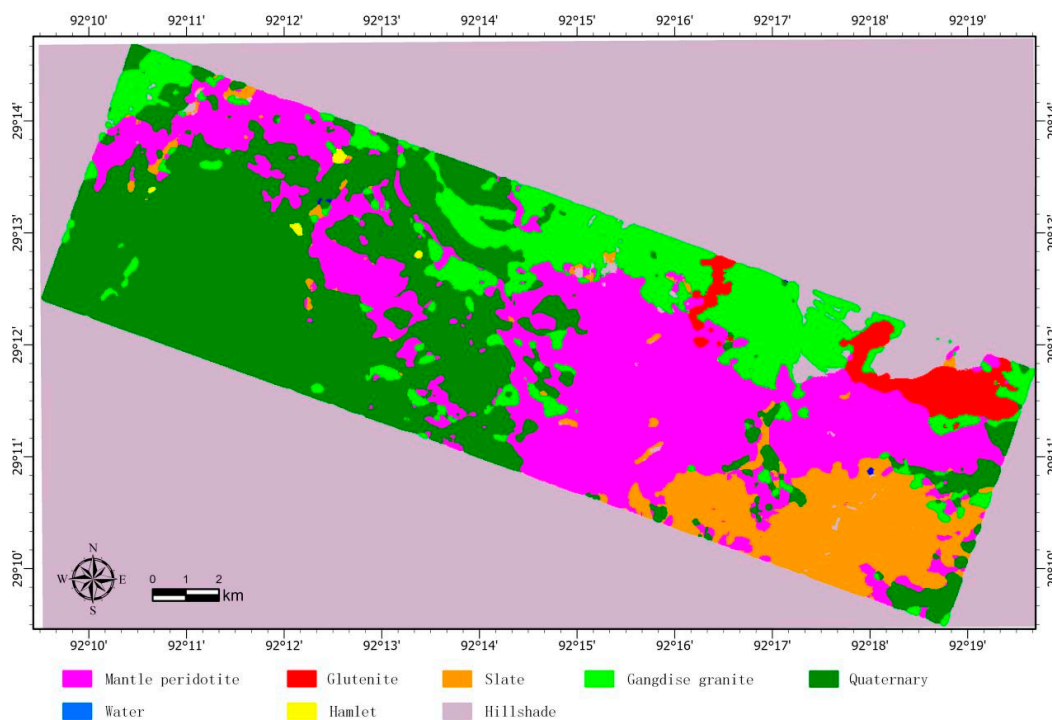


Figure 11. Lithological mapping using SVM classification based on Landsat8 OLI data.

5.3. Anomaly Extraction

Rocks and minerals containing groups such as Fe^{2+} or Fe^{3+} have characteristic spectral band shapes, which are mainly reflected in the visible bands. Fe^{3+} has strong absorption in the spectral range of $0.85\ \mu\text{m}\sim 0.94\ \mu\text{m}$ and appears as an absorption valley in the OLI 2 and OLI 5 bands. In remote-sensing images, it is shown by low brightness values. OLI 4 is the iron ion reflection band, which is shown as relatively bright in the OLI 4 image. The sign of the feature vector should be opposite to that of the coefficients of OLI 2 and OLI 5.

Because the visible light band is more sensitive to iron oxide, OLI 2, OLI 4, OLI 5, and OLI 6 are selected for principal component transformation to extract iron anomaly information, and OLI 7 is excluded to eliminate interference from hydroxyl or carbonate ion information. The criterion for judging the principal component representing the iron anomaly material is that the feature vector constituting this principal component should have an OLI 4 coefficient opposite in sign to the coefficients of OLI 2 and OLI 5, and generally has the same sign as the coefficients of OLI 6. Such a principal component is called an iron abnormal principal component. According to previous research, anomalies often appeared in the fourth principal component. The statistical analysis of the image feature vectors in the study area is shown in Table 3.

From Table 3, PC1 contains 88.96% of the information in the entire map, mainly reflecting brightness and terrain information, while PC4 only contains 0.39% of the information, but it represents abnormal information in the map. In order to obtain more accurate extraction results, the interference factors of mountain shadows and water bodies are eliminated using a mask file, and the fourth principal component where anomalies are concentrated is subjected to density segmentation. The result shows that the distribution of anomalies

matches well with the exposed mantle peridotite, indicating good indicative significance (Figure 12).

Table 3. Principal component analysis eigenvector matrix.

Eigenvectors	Band 2	Band 4	Band 5	Band 6	Information
PC1	−0.169	−0.348	−0.536	−0.750	88.96%
PC2	−0.611	−0.618	−0.087	0.487	9.71%
PC3	−0.390	−0.080	0.801	−0.447	0.94%
PC4	−0.668	0.700	−0.252	0.006	0.39%

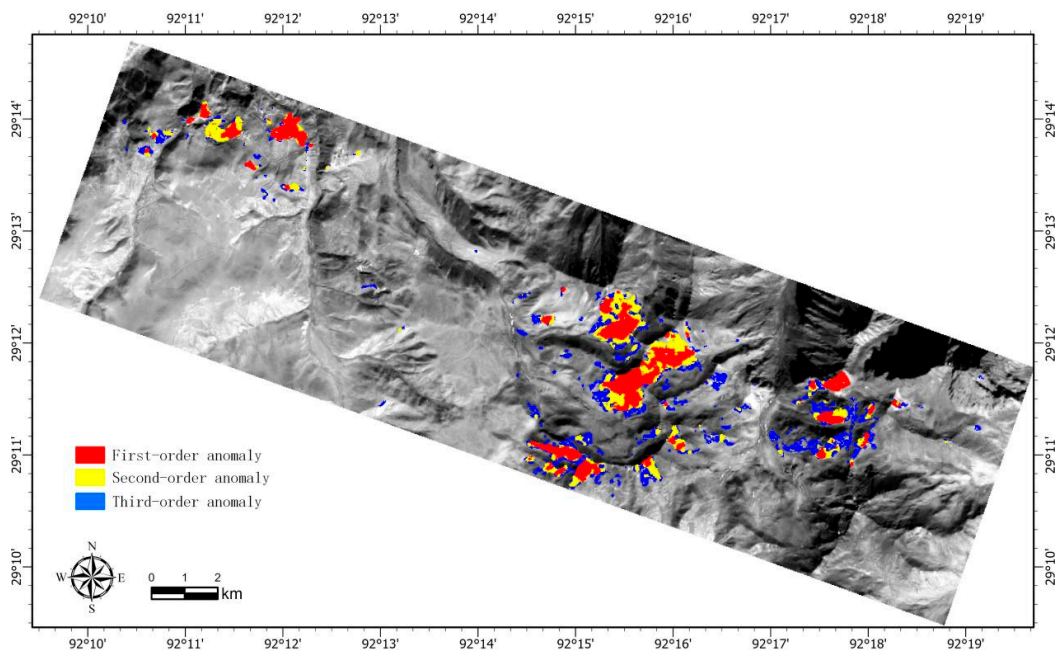


Figure 12. Abnormal extraction using de-interfered anomalous principal component thresholding technique based on Landsat8 OLI.

5.4. Field Geological Verification

Benefiting from the synergy of optical remote sensing and high spatial resolution imagery, the resulting lithological boundaries were acquired in a much shorter time compared to traditional geological surveys. Nevertheless, field-based geological mapping was still the backbone of the whole exploration procedure described in this study for verifying remote-sensing data.

The integrated OLI-WV2 results were utilized for the first time in the Luobusa area and proved their efficiency in lithological discrimination, as well as accurate detection of chrome-bearing peridotite and its spatially associated alteration. Fieldwork (field geology, field sampling, and field photos) as well as previous geological maps were used to validate remote sensing and machine learning results. Figure 13 shows the locations where the photos were taken for field verification.

The sedimentary rocks exposed in the study area are mainly located in the north of the ophiolite belt, composed of a set of rocks including polymictic conglomerate, sandstone, and greywacke. The conglomerate had strong weathering resistance, large terrain fluctuations, and rough textures (Figure 14a). The sandstone mostly formed a one-sided mountain; it appeared as inclined rock layers. They had a lower density of water systems and underdeveloped vegetation (Figure 14b,j). The field inspection results are consistent with the visual interpretation results of the WV-2 remote-sensing images (Figure 4a,b).

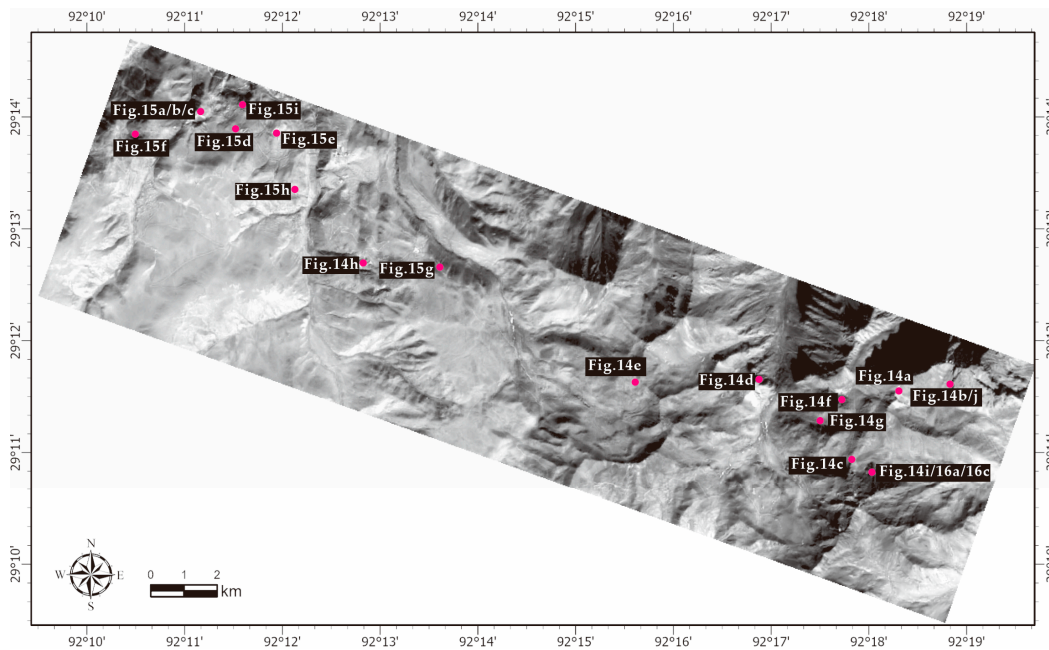


Figure 13. The OLI b5 image shows the field samples and figure locations in the study area.



Figure 14. Field photographs showing the rock units of (a) contacts between peridotite and Tertiary Luobusa Formation; (b) contacts between harzburgite, conglomerate, and sandstone; (c) outcrop of slate; (d) outcrop of harzburgite, Tertiary Luobusa Formation, and slate in Kangjinla; (e) a block of harzburgite; (f) contacts between harzburgite and dunite; (g) the view of chromite by open pit; (h) underground chromite mining; (i) quartz veins inside listwanite. (j) sandstone.

Currently, mining operations are still being carried out in the Luobusa mining area (Figure 14g,h). The chromite ore is mainly distributed in the harzburgite (Figure 15a,c–e). A clear contact boundary between dunite and harzburgite can be seen in the field (Figures 14f and 15g). The main rock-forming minerals of the two rocks are forsterite, and they have roughly similar spectral absorption characteristics. Therefore, they are uniformly identified as peridotites. The harzburgite has a blocky structure (Figure 14e), with severe surface weathering, and is mostly dark yellow-brown. The serpentinite peridotite is dark green in color, with obvious interpretation marks on the WV-2 true color image (Figure 6a,b). The gabbro was interlaced in veins (Figure 14f). Due to the later tectonic movement modification, the exposed range is not large and is difficult to identify on remote-sensing images.

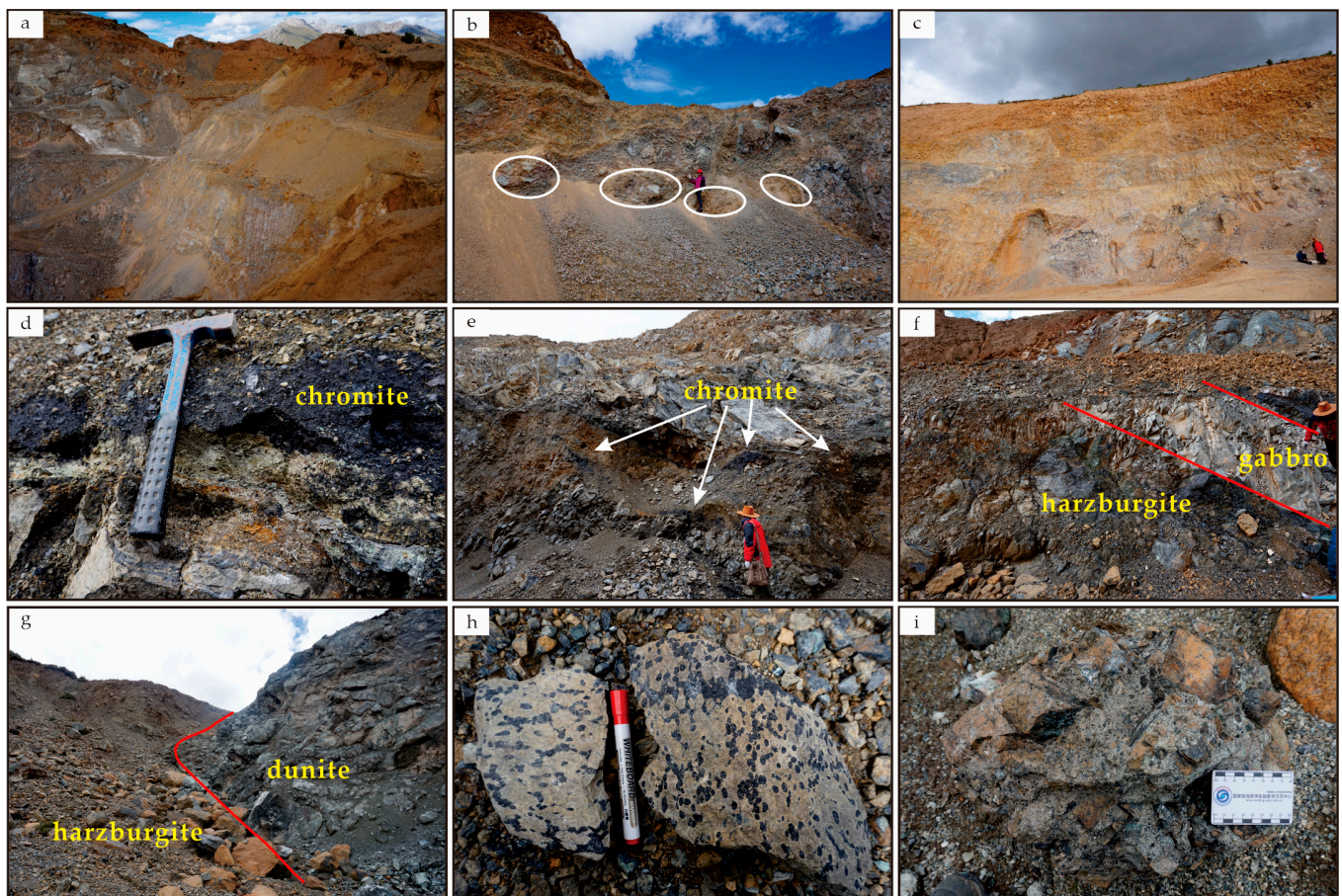


Figure 15. Field photographs showing the rock units of (a,c) the view of Luobusa by open pit; (b) structural lenticular body; (d,e) outcrop of chromite; (f) a block of gabbro; (g) contacts between harzburgite and dunite in Xiangkashan; (h) anti-nodular structure; (i) tectonic breccia.

The linear features in the study area were enhanced by directional filtering (Figure 16b, scale 1:50,000) to interpret the tectonic structures. Meanwhile, according to mineralogical research, the cataclastic structure is widely developed in the southeastern part of the study area, which indicates that the rocks may have undergone relatively strong tectonic stress [34,105]. In addition, the experimental petrological evidence shows that chromite in the Luobusa ophiolite is formed by the reaction between boninite melts and harzburgite. Boninite is a typical product of the forearc basin in island arc systems, and the subduction zone is the most favorable environment for finding podiform chromite ores. Therefore, the discovery of podiform chromite can even be used as a marker for determining the tectonic environment. The formation of podiform chromite is closely related to the formation of

ophiolites [41,42]. In recent years, a large number of ultra-high pressure minerals have been found in mantle peridotites and podiform chromites [10,45,106], suggesting that the formation depth of podiform chromite may reach the transition zone, and even the lower mantle [10,38]. Therefore, the formation process of Luobusa podiform chromite involves both deep and shallow processes, and may have undergone multiple stages of evolution, including from the transition zone, mid-ocean ridges, subduction zones, and even late-stage surface evolution [1,6]. The involvement of fluids in the mineralization process of podiform chromite favors the liquation of chromite and silicates, forming orientated chromite that indicates the direction of fluid movement (Figure 2c). Conversely, Figure 15h shows a reversed pisolitic structure, which also represents the hydrodynamic record [107]. The most direct evidence of the effect of tectonic structures on the spatial distribution of podiform chromite deposits is the east–west distribution of chromite ore belts caused by the convergence in the north–south direction, often accompanied by tectonic lenses and breccias [32,108,109] (Figures 15b,i and 16c).

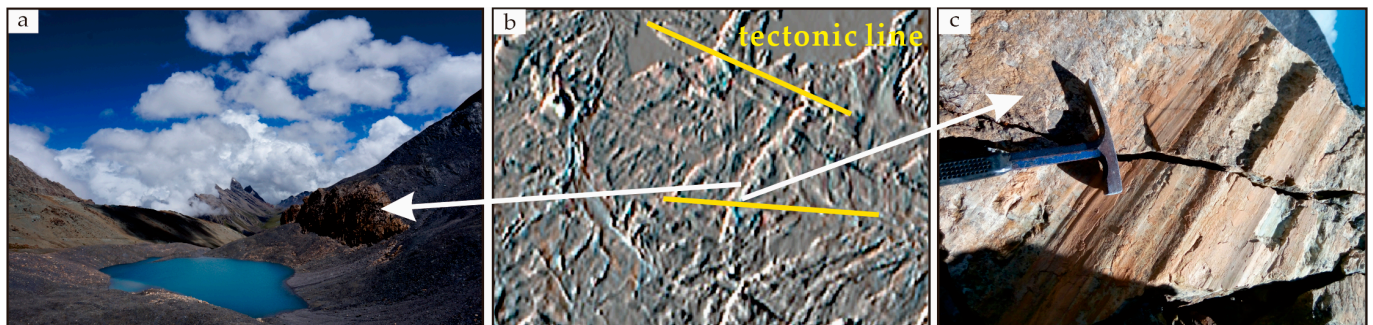


Figure 16. (a) Field photograph; (b) directional filtering of OLI image; (c) structure sliding plane.

The slate is distributed in the southern area of the ophiolite belt and is in a fault contact with ophiolite. It has a large outcrop area and is well exposed (Figure 14d). The WV-2 image clearly shows a large-scale reverse fault (Figure 5a). The quartz magnesite rock is distributed between the serpentinite ultramafic rock and the slate (Figure 14c). It is formed by the peridotites or serpentinite under the condition of carbon dioxide-rich hydrothermal activity. It can be divided into three alteration zones when observed in the field from north to south: peridotite zone, serpentinite zone, and quartz magnesite zone [110]. This has a good correspondence with the WV-2 image (Figure 5c) and shows the interpretation advantages of WV-2 high spatial resolution. The contact boundary between quartz magnesite and slate is clear, and they outcrop intermittently along the southern boundary of the ophiolite massifs (Figure 16a). Quartz and carbonate veins of varying widths (3–15 cm) are also developed in the quartz magnesite (Figure 14i).

6. Conclusions

The largest chromite deposit in China is located in the mantle peridotite of the Luobusa ophiolite. In this study, Landsat8 OLI multispectral and WorldView-2 high spatial resolution remote-sensing data have been employed to delineate the ophiolite complexes for exploring high-potential chromite zones using several image-processing techniques for the first time, which were proven to be successful in discriminating lithological units and delineating chromite host rock within ophiolites, especially in harsh plateau areas, and is of great significance for realizing modern geological surveys.

Seven spectral enhancement methods were comprehensively used to delineate mantle peridotites in the area, including decorrelation stretching, band ratio, ICA, PCA, MNF, and FCC, which detected different rock units and mantle peridotite as a host rock of chromitite within ophiolitic complexes at a regional scale. Meanwhile, the spatial resolution advantage of WorldView-2 remote-sensing data was used to establish interpretation signs for the main rock units in the study area. The support vector machine classification method was applied

to the digital Landsat multispectral OLI data, which gave rise to the supervised classified thematic map of the investigated area. The overall accuracy assessment of the produced classification map was accepted. At the same time, the “De-interfered Anomalous Principal Component Thresholding Technique” was used to extract abnormal information, and the result shows a good matching relationship with the chromite mineralized belt, especially in areas where ophiolitic peridotites are exposed, indicating good significance. Finally, image-processing results were verified by comprehensive fieldwork. The results of this study demonstrate the applicability of remote-sensing data for the delineation of harzburgite or peridotite as host rocks of chromite mineralization in the Luobusa zone and lithological mapping in mountainous and inaccessible regions.

Author Contributions: Conceptualization, W.Y.; methodology, W.Y.; software, W.Y.; validation, W.Y. and Y.Z. (Youye Zheng); formal analysis, W.Y.; investigation, W.Y.; resources, Y.Z. (Youye Zheng); data curation, W.Y.; writing—original draft preparation, W.Y.; writing—review and editing, S.C., X.X. and X.D.; visualization, W.Y.; supervision, Y.Z. (Youye Zheng); project administration, W.Y.; funding acquisition, Y.Z. (Yu Zhou). All authors have read and agreed to the published version of the manuscript.

Funding: This research was funded by Secondary Project of China Geological Survey [DD20211550] and Natural Science Foundation of Xinjiang Uygur Autonomous Region [2022D01A148].

Institutional Review Board Statement: Not applicable.

Informed Consent Statement: Not applicable.

Data Availability Statement: The datasets presented in this study can be obtained upon request to the corresponding author.

Acknowledgments: Constructive comments from the editors, and the revisions from anonymous reviewers greatly improved the manuscript of this paper.

Conflicts of Interest: The authors declare no conflict of interest.

References

- Xiong, F.; Yang, J.; Robinson, P.T.; Xu, X.; Liu, Z.; Li, Y.; Li, J.; Chen, S. Origin of podiform chromitite, a new model based on the Luobusa ophiolite, Tibet. *Gondwana Res.* **2015**, *27*, 525–542. [[CrossRef](#)]
- Wang, X.B.; Zhou, X.; Hao, Z.G. Some opinions on further exploration for chromite deposits in the Luobusha area, Tibet, China. *Geol. Bull. China* **2010**, *29*, 105–114.
- Pournamdari, M.; Hashim, M.; Pour, A.B. Application of ASTER and Landsat TM Data for Geological Mapping of Esfandagheh Ophiolite Complex, Southern Iran. *Resour. Geol.* **2014**, *64*, 233–246. [[CrossRef](#)]
- Xiong, F.H.; Yang, J.S.; Liu, Z.; Guo, G.L.; Chen, S.Y.; Xu, X.Z.; Li, Y.; Liu, F. High-Cr and high-Al chromitite found in western Yar-lung-Zangbo suture zone in Tibet. *Acta Petrol. Sin.* **2013**, *29*, 1878–1908.
- Yang, J.; Lian, D.; Wei, W.; Yang, Y.; Cai, P.; Rui, H.; Shi, R.; Xiong, F. Chromitites in ophiolites: Questions and thoughts. *Acta Geol. Sin.* **2022**, *96*, 1608–1634. [[CrossRef](#)]
- Xu, X.; Yang, J.; Robinson, P.T.; Xiong, F.; Ba, D.; Guo, G. Origin of ultrahigh pressure and highly reduced minerals in podiform chromitites and associated mantle peridotites of the Luobusa ophiolite, Tibet. *Gondwana Res.* **2015**, *27*, 686–700. [[CrossRef](#)]
- Zhang, P.-F.; Zhou, M.-F.; Malpas, J.; Robinson, P.T. Origin of high-Cr chromite deposits in nascent mantle wedges: Petrological and geochemical constraints from the Neo-Tethyan Luobusa ophiolite, Tibet. *Ore Geol. Rev.* **2020**, *123*, 103581. [[CrossRef](#)]
- He, Y.; Zhu, X.; She, Y.; Ma, J.; Sun, J.; Gao, Z.; Wan, H.; Chen, Y. Mechanism of formation of podiform chromitite: Insights from the oxidation states of podiform chromitites and host peridotites from the Luobusa ophiolite, southern Tibet. *Ore Geol. Rev.* **2021**, *139*, 104483. [[CrossRef](#)]
- Zhang, Q.; Ba, D.; Xiong, F.; Yang, J. Discussion on genesis process and deep prospecting breakthrough of Luobusa chromitite, Tibet. *Geol. China* **2017**, *44*, 224–241. [[CrossRef](#)]
- Yang, J.S.; Bai, W.J.; Fang, Q.S.; Rong, H. Ultrahigh-pressure Minerals and New Minerals from the Luobusa. *Acta Geosci.-Casinica* **2008**, *29*, 263–274. [[CrossRef](#)]
- Chung, Y.S.; Yoon, S.U.; Heo, S.; Kim, Y.S.; Kim, Y.-H.; Han, G.D.; Ahn, J. Classification of Tree Composition in the Forest Using Images from SENTINEL-2: A Case Study of Geomunoreum Forests Using NDVI Images. *Appl. Sci.* **2023**, *13*, 303. [[CrossRef](#)]
- Zheng, S.; An, Y.; Shi, P.; Zhao, T. Mapping the Lithological Features and Ore-controlling Structures Related to Ni–Cu Mineralization in the Eastern Tian Shan, NW China from ASTER Data. *Remote Sens.* **2021**, *13*, 206. [[CrossRef](#)]
- Ye, B.; Tian, S.; Cheng, Q.; Ge, Y. Application of Lithological Mapping Based on Advanced Hyperspectral Imager (AHSI) Imagery Onboard Gaofen-5 (GF-5) Satellite. *Remote. Sens.* **2020**, *12*, 3990. [[CrossRef](#)]

14. Tompolidi, A.-M.; Sykioti, O.; Koutroumbas, K.; Parcharidis, I. Spectral Unmixing for Mapping a Hydrothermal Field in a Volcanic Environment Applied on ASTER, Landsat-8/OLI, and Sentinel-2 MSI Satellite Multispectral Data: The Nisyros (Greece) Case Study. *Remote Sens.* **2020**, *12*, 4180. [[CrossRef](#)]
15. Eslami, A.; Ghaderi, M.; Rajendran, S.; Pour, A.B.; Hashim, M. Integration of ASTER and landsat TM remote sensing data for chromite prospecting and lithological mapping in Neyriz ophiolite zone, south Iran. *Resour. Geol.* **2015**, *65*, 375–388. [[CrossRef](#)]
16. Belgrano, T.M.; Diamond, L.W.; Novakovic, N.; Hewson, R.D.; Hecker, C.A.; Wolf, R.C.; Zieliński, L.d.D.; Kuhn, R.; Gilgen, S.A. Multispectral discrimination of spectrally similar hydrothermal minerals in mafic crust: A 5000 km² ASTER alteration map of the Oman–UAE ophiolite. *Remote Sens. Environ.* **2022**, *280*, 113211. [[CrossRef](#)]
17. Taha, A.M.M.; Xi, Y.; He, Q.; Hu, A.; Wang, S.; Liu, X. Investigating the Capabilities of Various Multispectral Remote Sensors Data to Map Mineral Prospectivity Based on Random Forest Predictive Model: A Case Study for Gold Deposits in Hamissana Area, NE Sudan. *Minerals* **2022**, *13*, 49. [[CrossRef](#)]
18. Eskandari, A.; Hosseini, M.; Nicotra, E. Application of Satellite Remote Sensing, UAV-Geological Mapping, and Machine Learning Methods in the Exploration of Podiform Chromite Deposits. *Minerals* **2023**, *13*, 251. [[CrossRef](#)]
19. Dong, X.; Gan, F.; Li, N.; Zhang, S.; Li, T. Mineral mapping in the Duolong porphyry and epithermal ore district, Tibet, using the Gaofen-5 satellite hyperspectral remote sensing data. *Ore Geol. Rev.* **2022**, *151*, 105222. [[CrossRef](#)]
20. Rothery, D.A. Improved discrimination of rock units using Landsat Thematic Mapper imagery of the Oman ophiolite. *J. Geol. Soc. London* **1987**, *144*, 587–597. [[CrossRef](#)]
21. Xiong, Y.; Khan, S.D.; Mahmood, K.; Sisson, V.B. Lithological mapping of Bela ophiolite with remote-sensing data. *Int. J. Remote Sens.* **2011**, *32*, 4641–4658. [[CrossRef](#)]
22. Abrams, M.; Rothery, D.; Pontual, A. Mapping in the Oman ophiolite using enhanced Landsat Thematic Mapper images. *Tectonophysics* **1988**, *151*, 387–401. [[CrossRef](#)]
23. Khan, S.D.; Mahmood, K.; Casey, J.F. Mapping of Muslim Bagh ophiolite complex (Pakistan) using new remote sensing, and field data. *J. Asian Earth Sci.* **2007**, *30*, 333–343. [[CrossRef](#)]
24. Sultan, M.; Arvidson, R.E.; Sturchio, N.C. Mapping of serpentinites in the Eastern Desert of Egypt by using Landsat thematic mapper data. *Geology* **1986**, *14*, 995–999. [[CrossRef](#)]
25. Khan, S.D.; Mahmood, K. The application of remote sensing techniques to the study of ophiolites. *Earth-Sci. Rev.* **2008**, *89*, 135–143. [[CrossRef](#)]
26. Muthamilselvan, A. Application of Supervised Classification and Crosta Technique for Lithological Discrimination in Parts of South Khetri Belt, Sikar District, Rajasthan. *J. Indian Soc. Remote Sens.* **2016**, *45*, 377–383. [[CrossRef](#)]
27. Othman, A.A.; Gloaguen, R. Integration of spectral, spatial and morphometric data into lithological mapping: A comparison of different Machine Learning Algorithms in the Kurdistan Region, NE Iraq. *J. Asian Earth Sci.* **2017**, *146*, 90–102. [[CrossRef](#)]
28. Abdul-Qadir, A.M. Supervised Classification for Lithologic Discrimination in Shaikh Ibrahim Area, NW Iraq Using Landsat Images. *Arab. J. Sci. Eng.* **2014**, *39*, 437–451. [[CrossRef](#)]
29. Rajendran, S.; Nasir, S. Mapping of Moho and Moho Transition Zone (MTZ) in Samail ophiolites of Sultanate of Oman using remote sensing technique. *Tectonophysics* **2015**, *657*, 63–80. [[CrossRef](#)]
30. Xu, X.; Zoheir, B.; Yang, J.; Xiong, F.; Guo, G.; Feng, G.; Li, Z.; Li, T. Tectonized Neotethyan lithosphere in southeastern Tibet: Results of the Luobusa ophiolite drilling. *Lithos* **2023**, *436–437*, 106947. [[CrossRef](#)]
31. Zhang, C.; Liu, C.-Z.; Liu, T.; Wu, F.-Y. Evolution of mantle peridotites from the Luobusa ophiolite in the Tibetan Plateau: Sr-Nd-Hf-Os isotope constraints. *Lithos* **2020**, *362–363*, 105477. [[CrossRef](#)]
32. Yamamoto, H.; Yamamoto, S.; Kaneko, Y.; Terabayashi, M.; Komiya, T.; Katayama, I.; Iizuka, T. Imbricate structure of the Luobusa Ophiolite and surrounding rock units, southern Tibet. *J. Asian Earth Sci.* **2007**, *29*, 296–304. [[CrossRef](#)]
33. Hébert, R.; Bezaud, R.; Guilmette, C.; Dostal, J.; Wang, C.; Liu, Z. The Indus–Yarlung Zangbo ophiolites from Nanga Parbat to Namche Barwa syntaxes, southern Tibet: First synthesis of petrology, geochemistry, and geochronology with incidences on geodynamic reconstructions of Neo-Tethys. *Gondwana Res.* **2012**, *22*, 377–397. [[CrossRef](#)]
34. Xu, X.; Yang, J.; Ba, D.; Guo, G.; Robinson, P.T.; Li, J. Petrogenesis of the Kangjinla peridotite in the Luobusa ophiolite, Southern Tibet. *J. Asian Earth Sci.* **2011**, *42*, 553–568. [[CrossRef](#)]
35. Xu, X.; Yang, J.; Chen, S.; Fang, Q.; Bai, W.; Ba, D. Unusual mantle mineral group from chromitite orebody Cr-11 in Luobusa ophiolite of Yarlung–Zangbo suture zone, Tibet. *J. Earth Sci.–China* **2009**, *20*, 284–302. [[CrossRef](#)]
36. Fahui, X.; Jingsui, Y.; Yuan, L.; Zhao, L.; Guolin, G.; Wenda, Z.; Songyong, C.; Yibing, L.; Xiangzhen, X.; Xiaolu, N. Tectonic Setting of Dongbo Ophiolite in the Western Portion of the Yarlung Zangbo Suture Zone, Tibet. *Acta Geosci. Sinica* **2015**, *36*, 31–40. [[CrossRef](#)]
37. Liang, F.; Yang, J.; Xu, Z.; Zhao, J. Chromium in the olivine lattice: Chromium-rich olivines and their implication of deep mantle origin in the Luobusa mantle peridotite and chromitite, Tibet. *Acta Petrol. Sin.* **2014**, *30*, 2125–2136.
38. Xiong, F.; Yang, J.; Liu, Z. Multi-stage formation of the podiform chromitite. *Geol. China* **2013**, *40*, 820–839. [[CrossRef](#)]
39. Shi, R.; Alard, O.; Zhi, X.; O’Reilly, S.Y.; Pearson, N.J.; Griffin, W.L.; Zhang, M.; Chen, X. Multiple events in the Neo-Tethyan oceanic upper mantle: Evidence from Ru–Os–Ir alloys in the Luobusa and Dongqiao ophiolitic podiform chromitites, Tibet. *Earth Planet. Sci. Lett.* **2007**, *261*, 33–48. [[CrossRef](#)]
40. Liu, C.-Z.; Wu, F.-Y.; Wilde, S.A.; Yu, L.-J.; Li, J.-L. Anorthitic plagioclase and pargasitic amphibole in mantle peridotites from the Yungbwa ophiolite (southwestern Tibetan Plateau) formed by hydrous melt metasomatism. *Lithos* **2010**, *114*, 413–422. [[CrossRef](#)]

41. Zhou, E. Present situation and advances in the study of podiform chromite deposits. *Acta Petrol.-Aologica* **2011**, *30*, 530–542. [[CrossRef](#)]
42. Erbin, Z.; Zhuse, Y.; Wan, J.; Zengqian, H.; Fusheng, G.; Jun, H. Study on mineralogy of Cr-spinel and genesis of Luobusha chromite deposit in South Tibet. *Acta Petrol. Sin.* **2011**, *27*, 2060–2072.
43. Guo, G.L.; Yang, J.S.; Liu, X.D.; Xu, X.Z.; Wu, Y. In situ research on PGM in Luobusha ophiolitic chromitites, Tibet: Implications for the crystallization of the chromite. *Acta Petrol. Sin.* **2016**, *32*, 3673–3684.
44. Yang, J.; Xu, X.; Zhang, Z.; Rong, H.; Liu, Y.; Xiong, F.; Liang, F.; Liu, Z.; Liu, F.; Li, J.; et al. Ophiolite-type Diamond and Deep Genesis of Chromitite. *Acta Geosci. Sin.* **2013**, *34*, 643–653. [[CrossRef](#)]
45. Bai, W.J.; Yang, J.S.; Shi, N.C.; Fang, Q.S.; Dai, M.Q.; Xiong, M.; Yan, B.G. A Discovery of Ultrahigh Pressure Minerals-Wustite and Native Iron from the Mantle Ophiolite, at Luobusha, Tibet. *Geol. Rev.* **2004**, *50*, 184–188. [[CrossRef](#)]
46. Masoumi, F.; Eslamkish, T.; Honarmand, M.; Abkar, A.A. A Comparative Study of Landsat-7 and Landsat-8 Data Using Image Processing Methods for Hydrothermal Alteration Mapping. *Resour. Geol.* **2017**, *67*, 72–88. [[CrossRef](#)]
47. Roy, D.P.; Wulder, M.A.; Loveland, T.R.; Woodcock, C.E.; Allen, R.G.; Anderson, M.C.; Helder, D.; Irons, J.R.; Johnson, D.M.; Kennedy, R.; et al. Landsat-8: Science and product vision for terrestrial global change research. *Remote Sens. Environ.* **2014**, *145*, 154–172. [[CrossRef](#)]
48. Nwaila, G.T.; Zhang, S.E.; Bourdeau, J.E.; Ghorbani, Y.; Carranza, E.J.M. Artificial intelligence-based anomaly detection of the Assen iron deposit in South Africa using remote sensing data from the Landsat-8 Operational Land Imager. *Artif. Intell. Geosci.* **2022**, *3*, 71–85. [[CrossRef](#)]
49. Oikonomidis, D.; Vavelidis, M.; Melfos, V.; Artashova, M. Searching for ancient gold mines in Filippoi area, Macedonia, Greece, using Worldview-2 satellite imagery. *Geocarto Int.* **2017**, *32*, 87–96. [[CrossRef](#)]
50. Martin, J.; Eugenio, F.; Marcello, J.; Medina, A. Automatic Sun Glint Removal of Multispectral High-Resolution Worldview-2 Imagery for Retrieving Coastal Shallow Water Parameters. *Remote Sens.* **2016**, *8*, 37. [[CrossRef](#)]
51. Grebby, S.; Cunningham, D.; Tansey, K.; Naden, J. The Impact of Vegetation on Lithological Mapping Using Airborne Multispectral Data: A Case Study for the North Troodos Region, Cyprus. *Remote Sens.* **2014**, *6*, 10860–10887. [[CrossRef](#)]
52. Evans, D.J.A.; Ewertowski, M.; Jamieson, S.S.R.; Orton, C. Surficial geology and geomorphology of the Kumtor Gold Mine, Kyrgyzstan: Human impacts on mountain glacier landsystems. *J. Maps* **2016**, *12*, 757–769. [[CrossRef](#)]
53. Xie, C.; Huang, X.; Zeng, W.; Fang, X. A novel water index for urban high-resolution eight-band WorldView-2 imagery. *Int. J. Digit. Earth* **2016**, *9*, 925–941. [[CrossRef](#)]
54. Rapinel, S.; Clément, B.; Magnanon, S.; Sellin, V.; Hubert-Moy, L. Identification and mapping of natural vegetation on a coastal site using a Worldview-2 satellite image. *J. Environ. Manag.* **2014**, *144*, 236–246. [[CrossRef](#)] [[PubMed](#)]
55. Chander, G.; Markham, B.L.; Helder, D.L. Summary of current radiometric calibration coefficients for Landsat MSS, TM, ETM+, and EO-1 ALI sensors. *Remote Sens. Environ.* **2009**, *113*, 893–903. [[CrossRef](#)]
56. Elahi, F.; Muhammad, K.; Din, S.U.; Khan, M.F.A.; Bashir, S.; Hanif, M. Lithological Mapping of Kohat Basin in Pakistan Using Multispectral Remote Sensing Data: A Comparison of Support Vector Machine (SVM) and Artificial Neural Network (ANN). *Appl. Sci.* **2022**, *12*, 12147. [[CrossRef](#)]
57. Hashim, M.; Ahmad, S.; Md Johari, M.A.; Pour, A.B. Automatic lineament extraction in a heavily vegetated region using Landsat Enhanced Thematic Mapper (ETM+) imagery. *Adv. Space Res.* **2013**, *51*, 874–890. [[CrossRef](#)]
58. Benomar, T.; Fuling, B. Improved geological mapping using landsat-5 TM data in Weixi area, Yunnan province China. *Geo-Spat. Inf. Sci.* **2005**, *8*, 110–114. [[CrossRef](#)]
59. Gad, S.; Kusky, T. Lithological mapping in the Eastern Desert of Egypt, the Barramiya area, using Landsat thematic mapper (TM). *J. Afr. Earth Sci.* **2006**, *44*, 196–202. [[CrossRef](#)]
60. Mwaniki, M.W.; Matthias, M.S.; Schellmann, G. Application of Remote Sensing Technologies to Map the Structural Geology of Central Region of Kenya. *IEEE J. Sel. Top. Appl. Earth Obs. Remote Sens.* **2015**, *8*, 1855–1867. [[CrossRef](#)]
61. Rajendran, S.; Al-Khirbash, S.; Pracejus, B.; Nasir, S.; Al-Abri, A.H.; Kusky, T.M.; Ghulam, A. ASTER detection of chromite bearing mineralized zones in Semail Ophiolite Massifs of the northern Oman Mountains: Exploration strategy. *Ore Geol. Rev.* **2012**, *44*, 121–135. [[CrossRef](#)]
62. Yang, W.; Zheng, Y.; Liu, T.; Wang, P.; Wang, C.; Feng, Q.; Guo, T. The Application of High Spatial Resolution Data to Remote Sensing Geological Survey in the Luobusha Area, Tibet. *Geoscience* **2017**, *31*, 1284–1293. [[CrossRef](#)]
63. Yang, W.; Zheng, Y.; Liu, T.; Wang, P.; Guo, T. Delineation of peridotites in Luobusha, Tibet with remote sensing data based on spectral enhancement technology. *Miner. Explor.* **2018**, *9*, 158–164.
64. Panchal, S.; Thakker, R. Implementation and Comparative Quantitative Assessment of Different Multispectral Image Pan-sharpening Approaches. *Signal Image Process. Int. J.* **2015**, *6*, 35–48. [[CrossRef](#)]
65. Ruizi, Z.; Min, Z.; Jianping, C. Study on Geological Structural Interpretation Based on Worldview-2 Remote Sensing Image and Its Implementation. *Procedia Environ. Sci.* **2011**, *10*, 653–659. [[CrossRef](#)]
66. Cheng, G.; Huang, H.; Li, H.; Deng, X.; Khan, R.; Soh Tamehe, L.; Atta, A.; Lang, X.; Guo, X. Quantitative Remote Sensing of Metallic Elements for the Qishitan Gold Polymetallic Mining Area, NW China. *Remote Sens.* **2021**, *13*, 2519. [[CrossRef](#)]
67. Yang, W.; Zheng, Y.; Liu, T.; Wang, C. Remote Sensing Monitoring on Mine of WorldView-2 Satellite: A Case Study of the Luobusha Area, Tibet. *Geoscience* **2018**, *32*, 392–397. [[CrossRef](#)]
68. Chavez, J.P. Image Processing techniques for Thematic Mapper data. *Proc. ASPRS-ACSM Tech. Pap.* **1984**, *2*, 728–742.

69. Abdelkader, M.A.; Watanabe, Y.; Shebl, A.; El-Dokouny, H.A.; Dawoud, M.; Csámer, A. Effective delineation of rare metal-bearing granites from remote sensing data using machine learning methods: A case study from the Umm Naggat Area, Central Eastern Desert, Egypt. *Ore Geol. Rev.* **2022**, *150*, 105184. [[CrossRef](#)]
70. Khan, M.F.A.; Muhammad, K.; Bashir, S.; Din, S.U.; Hanif, M. Mapping Allochemical Limestone Formations in Hazara, Pakistan Using Google Cloud Architecture: Application of Machine-Learning Algorithms on Multispectral Data. *ISPRS Int. J. Geo-Inf.* **2021**, *10*, 58. [[CrossRef](#)]
71. Pournamdari, M.; Hashim, M. Detection of chromite bearing mineralized zones in Abdasht ophiolite complex using ASTER and ETM+ remote sensing data. *Arab. J. Geosci.* **2014**, *7*, 1973–1983. [[CrossRef](#)]
72. Bishta, A.Z.; Sonbul, A.R.; Qudsi, I.Z. Utilizing the image processing techniques in mapping the geology of Al Taif area, central western Arabian Shield, Saudi Arabia. *Arab. J. Geosci.* **2015**, *8*, 4161–4175. [[CrossRef](#)]
73. Kusky, T.M.; Ramadan, T.M. Structural controls on Neoproterozoic mineralization in the South Eastern Desert, Egypt: An integrated field, Landsat TM, and SIR-C/X SAR approach. *J. Afr. Earth Sci.* **2002**, *35*, 107–121. [[CrossRef](#)]
74. Bolouki, S.M.; Ramazi, H.R.; Maghsoudi, A.; Beiranvand Pour, A.; Sohrabi, G. A Remote Sensing-Based Application of Bayesian Networks for Epithermal Gold Potential Mapping in Ahar-Arasbaran Area, NW Iran. *Remote Sens.* **2020**, *12*, 105. [[CrossRef](#)]
75. Ibrahim, W.; Watanabe, K.; Yonezu, K. Structural and litho-tectonic controls on Neoproterozoic base metal sulfide and gold mineralization in North Hamisana shear zone, South Eastern Desert, Egypt: The integrated field, structural, Landsat 7 ETM + and ASTER data approach. *Ore Geol. Rev.* **2016**, *79*, 62–77. [[CrossRef](#)]
76. Van der Meer, F. Mapping the degree of serpentinization within ultramafic rock bodies using imaging spectrometer data. *J. Rock Mech. Min. Sci. Géoméch. Abstr.* **1995**, *32*, 330. [[CrossRef](#)]
77. Inzana, J.; Kusky, T.; Higgs, G.; Tucker, R. Supervised classifications of Landsat TM band ratio images and Landsat TM band ratio image with radar for geological interpretations of central Madagascar. *J. Afr. Earth Sci.* **2003**, *37*, 59–72. [[CrossRef](#)]
78. ElGalladi, A.; Araffa, S.; Mekkawi, M.; Abd-AlHai, M. Exploring mineralization zones using remote sensing and aeromagnetic data, West Allaqi Area, Eastern-Desert, Egypt. *Egypt. J. Remote Sens. Space Sci.* **2022**, *25*, 417–433. [[CrossRef](#)]
79. Liu, L.; Zhou, J.; Jiang, D.; Zhuang, D.; Mansaray, L.R. Lithological discrimination of the mafic-ultramafic complex, Huitongshan, Beishan, China: Using ASTER data. *J. Earth Sci.-China* **2014**, *25*, 529–536. [[CrossRef](#)]
80. Chen, Q.; Xia, J.; Zhao, Z.; Zhou, J.; Zhu, R.; Zhang, R.; Zhao, X.; Chao, J.; Zhang, X.; Zhang, G. Interpretation of hydrothermal alteration and structural framework of the Huize Pb–Zn deposit, SW China, using Sentinel-2, ASTER, and Gaofen-5 satellite data: Implications for Pb–Zn exploration. *Ore Geol. Rev.* **2022**, *150*, 105154. [[CrossRef](#)]
81. El-Wahed, M.A.; Kamh, S.; Abu Anbar, M.; Zoheir, B.; Hamdy, M.; Abdeldayem, A.; Lebda, E.M.; Attia, M. Multisensor Satellite Data and Field Studies for Unravelling the Structural Evolution and Gold Metallogeny of the Gerf Ophiolitic Nappe, Eastern Desert, Egypt. *Remote Sens.* **2023**, *15*, 1974. [[CrossRef](#)]
82. Sekandari, M.; Masoumi, I.; Pour, A.B.; Muslim, A.M.; Rahmani, O.; Hashim, M.; Zoheir, B.; Pradhan, B.; Misra, A.; Aminpour, S.M. Application of Landsat-8, Sentinel-2, ASTER and WorldView-3 Spectral Imagery for Exploration of Carbonate-Hosted Pb-Zn Deposits in the Central Iranian Terrane (CIT). *Remote Sens.* **2020**, *12*, 1239. [[CrossRef](#)]
83. Bentahar, I.; Raji, M. Comparison of Landsat OLI, ASTER, and Sentinel 2A data in lithological mapping: A Case study of Rich area (Central High Atlas, Morocco). *Adv. Space Res.* **2021**, *67*, 945–963. [[CrossRef](#)]
84. Wang, J.; Chang, C.-I. Independent component analysis-based dimensionality reduction with applications in hyperspectral image analysis. *IEEE Trans. Geosci. Remote Sens.* **2015**, *6*, 600–665. [[CrossRef](#)]
85. Pour, A.B.; Hashim, M.; Hong, J.K.; Park, Y. Lithological and alteration mineral mapping in poorly exposed lithologies using Landsat-8 and ASTER satellite data: North-eastern Graham Land, Antarctic Peninsula. *Ore Geol. Rev.* **2019**, *108*, 112–133. [[CrossRef](#)]
86. Kumar, C.; Chatterjee, S.; Oommen, T.; Guha, A. Automated lithological mapping by integrating spectral enhancement techniques and machine learning algorithms using AVIRIS-NG hyperspectral data in Gold-bearing granite-greenstone rocks in Hutti, India. *Int. J. Appl. Earth Obs. Geoinform.* **2020**, *86*, 102006. [[CrossRef](#)]
87. Gabr, S.S.; Hassan, S.M.; Sadek, M.F. Prospecting for new gold-bearing alteration zones at El-Hoteib area, South Eastern Desert, Egypt, using remote sensing data analysis. *Ore Geol. Rev.* **2015**, *71*, 1–13. [[CrossRef](#)]
88. Pour, A.B.; Hashim, M.; Pournamdari, M. Chromitite prospecting using landsat tm and aster remote sensing data. *ISPRS Ann. Photogramm. Remote Sens. Spat. Inf. Sci.* **2015**, *II-2/W2*, 99–103. [[CrossRef](#)]
89. Shirmard, H.; Farahbakhsh, E.; Müller, R.D.; Chandra, R. A review of machine learning in processing remote sensing data for mineral exploration. *Remote Sens. Environ.* **2022**, *268*, 112750. [[CrossRef](#)]
90. Pal, M.; Mather, P.M. Support vector machines for classification in remote sensing. *Int. J. Remote Sens.* **2005**, *26*, 1007–1011. [[CrossRef](#)]
91. Puertas, O.L.; Brenning, A.; Meza, F.J. Balancing misclassification errors of land cover classification maps using support vector machines and Landsat imagery in the Maipo river basin (Central Chile, 1975–2010). *Remote Sens. Environ.* **2013**, *137*, 112–123. [[CrossRef](#)]
92. Yousefi, M.; Tabatabaei, S.H.; Rikhtehgaran, R.; Pour, A.B.; Pradhan, B. Application of Dirichlet Process and Support Vector Machine Techniques for Mapping Alteration Zones Associated with Porphyry Copper Deposit Using ASTER Remote Sensing Imagery. *Minerals* **2021**, *11*, 1235. [[CrossRef](#)]

93. Othman, A.A.; Gloaguen, R. Improving Lithological Mapping by SVM Classification of Spectral and Morphological Features: The Discovery of a New Chromite Body in the Mawat Ophiolite Complex (Kurdistan, NE Iraq). *Remote Sens.* **2014**, *6*, 6867–6896. [[CrossRef](#)]
94. Rodriguez-Galiano, V.; Sanchez-Castillo, M.; Chica-Olmo, M.; Chica-Rivas, M.J. Machine learning predictive models for mineral prospectivity: An evaluation of neural net-works, random forest, regression trees and support vector machines. *Ore Geol. Rev.* **2015**, *71*, 804–818. [[CrossRef](#)]
95. Shabankareh, M.; Hezarkhani, A. Application of support vector machines for copper potential mapping in Kerman region, Iran. *J. Afr. Earth Sci.* **2015**, *118*, 116–126. [[CrossRef](#)]
96. Zhang, Y.; Zeng, C. Study of optimum discriminator of multi-channel remote sensing anomaly for recognition of porphyry Cu deposits in Gangdese belt. *Miner. Depos.* **2012**, *31*, 671–698.
97. Gan, F.P.; Wang, R.S.; Ma, A.N.; Zhang, Z.G.; Li, M.X. Integration for Extracting and Mineral Analysis Models for Geological Application Using Remote Sensing Data. *J. Remote Sens.* **2003**, *7*, 207–213. [[CrossRef](#)]
98. Pournamdari, M.; Hashim, M.; Pour, A.B. Spectral transformation of ASTER and Landsat TM bands for lithological mapping of Soghan ophiolite complex, south Iran. *Adv. Space Res.* **2014**, *54*, 694–709. [[CrossRef](#)]
99. Abdelaziz, R.; El-Rahman, Y.A.; Wilhelm, S. Landsat-8 data for chromite prospecting in the Logar Massif, Afghanistan. *Heliyon* **2018**, *4*, e00542. [[CrossRef](#)]
100. Sonbul, A.R.; El-Shafei, M.K.; Bishta, A.Z. Using remote sensing techniques and field-based structural analysis to explore new gold and associated mineral sites around Al-Hajar mine, Asir terrane, Arabian Shield. *J. Afr. Earth Sci.* **2016**, *117*, 285–302. [[CrossRef](#)]
101. Mehdikhani, B.; Imamalipour, A. ASTER-Based Remote Sensing Image Analysis for Prospection Criteria of Podiform Chromite at the Khoy Ophiolite (NW Iran). *Minerals* **2021**, *11*, 960. [[CrossRef](#)]
102. Crosta, A.P.; De Filho, C.R.S.; Azevedo, F.; Brodie, C. Targeting key alteration minerals in epithermal deposits in Patagonia, Argentina, using ASTER imagery and principal component analysis. *Int. J. Remote Sens.* **2003**, *24*, 4233–4240. [[CrossRef](#)]
103. Zoheir, B.; Emam, A. Integrating geologic and satellite imagery data for high-resolution mapping and gold exploration targets in the South Eastern Desert, Egypt. *J. Afr. Earth Sci.* **2012**, *66–67*, 22–34. [[CrossRef](#)]
104. Ahmadfaraj, M.; Mirmohammadi, M.; Afzal, P. Application of fractal modeling and PCA method for hydrothermal alteration mapping in the Saveh area (Central Iran) based on ASTER multispectral data. *Int. J. Min. Geo-Eng.* **2016**, *50*, 37–48. [[CrossRef](#)]
105. Robinson, P.T.; Trumbull, R.B.; Schmitt, A.; Yang, J.-S.; Li, J.-W.; Zhou, M.-F.; Erzinger, J.; Dare, S.; Xiong, F. The origin and significance of crustal minerals in ophiolitic chromitites and peridotites. *Gondwana Res.* **2015**, *27*, 486–506. [[CrossRef](#)]
106. Bai, W.J.; Yang, J.S.; Fang, Q.S. Zhang. Study on a storehouse of ultrahigh pressure mantle minerals—Podiform chromite deposits. *Earth Sci. Front.* **2001**, *8*, 111–121. [[CrossRef](#)]
107. Luo, Z.; Jiang, X.; Liu, X.; Li, Z.; Wu, Z.; Jing, W. Imprints of fluid process of shell dunite in ophiolitic chromite deposits: Evidences from geology, petrology and crystal chemistry of olivine found in Luobusa and Zedang ophiolites in the Yarlung Zangbo suture zone, Tibet. *Earth Sci. Front.* **2019**, *26*, 272–285. [[CrossRef](#)]
108. Li, D. Mantleshear Mineralization of Luobushachromites, Tibet. *Chin. J. Nonferrous Met.* **1997**, *7*, 4–8.
109. Li, D. Structural processes of metallogenic evolution of luobusha chromite deposits. *Geoscience* **1995**, *9*, 450–458.
110. Zhang, L.; Yang, J.; Paul, T. Origin of Listwanite in the Luobusa Ophiolite, Tibet, Implications for Chromite Stability in Hydrothermal Systems. *Acta Geol. Sin.* **2015**, *89*, 402–417.

Disclaimer/Publisher’s Note: The statements, opinions and data contained in all publications are solely those of the individual author(s) and contributor(s) and not of MDPI and/or the editor(s). MDPI and/or the editor(s) disclaim responsibility for any injury to people or property resulting from any ideas, methods, instructions or products referred to in the content.